Perfectly zoned sphaerosiderite

1   # Groundwater table fluctuations recorded in zonation of microbial

2   # siderites from end-Triassic strata

3

4   By Weibel, R.[1*], Lindström, S. [1], Pedersen, G. K. [1], Johansson, L. [2] Dybkjær, K. [1], Whitehouse, M. [3],

5   Boyce, A.[4], Leng, M.J.[5]

6

7

8   [1] GEUS, Geological Survey of Denmark and Greenland, Øster Voldgade 10, 1350 Copenhagen K, Denmark.

9   [2] Department of Geology, Lund University, Sölvegatan 12, 223 62 Lund, Sweden.

10   [3] Department of Geosciences, Naturhistoriska Riksmuseet, 104 05 Stockholm, Sweden.

11   [4] NERC Isotope Geosciences Facilities, SUERC, Rankine Avenue, East Kilbride, G75 0QF, UK.

12   [5] NERC Isotope Geosciences Facilities (Stable Isotope Facility), British Geological Survey, Keyworth,

13   Nottingham, NG12 5GG, UK.

14

15   *Corresponding author: Weibel, R., rwh@geus.dk, Phone: +45 51513364

16

17

18   ## Keywords

19   Siderite concretions; sphaerosiderite; spheroidal siderite; oxygen and carbon isotopic composition; microbial

20   activity; groundwater fluctuations

21

22

23

24

Abstract

In a terrestrial Triassic–Jurassic boundary succession of southern Sweden, perfectly zoned sphaerosiderites are restricted to a specific sandy interval deposited during the end-Triassic event. Underlying and overlying this sand interval there are several other types of siderite micromorphologies, i.e. poorly zoned sphaerosiderite, spheroidal (ellipsoid) siderite, spherical siderite and rhombohedral siderite. Siderite overgrowths occur mainly as rhombohedral crystals on perfectly zoned sphaerosiderite and as radiating fibrous crystals on spheroidal siderite. Concretionary sparry, microspar and/or micritic siderite cement postdate all of these micromorphologies. The carbon isotope composition of the siderite measured by conventional mass spectrometry shows the characteristic broad span of data, probably as a result of multiple stages of microbial activity. SIMS (secondary ion mass spectrometry) revealed generally higher $\delta^{13}C$ values for the concretionary cement than the perfectly zoned sphaerosiderite, spheroidal siderite and their overgrowths, which marks a change in the carbon source during burial. All the various siderite morphologies have almost identical oxygen isotope values reflecting the palaeo-groundwater composition. A pedogenic / freshwater origin is supported by the trace element compositions of varying Fe:Mn ratios and low Mg contents. Fluctuating groundwater is the most likely explanation for uniform repeated siderite zones of varying Fe:Mn ratios reflecting alternating physiochemical conditions and hostility to microbial life/activity. Bacterially-mediated siderite precipitation likely incorporated Mn and other metal ions during conditions that are not favourable for the bacteria and continued with Fe-rich siderite precipitation as the physico-chemical conditions changed into optimal conditions again, reflecting the response to groundwater fluctuations.

Introduction

50

51

52 Siderite is a common early diagenetic mineral occurring with a variety of morphologies in different

53 depositional environments. Rhombohedral and spheroidal (ellipsoid-shaped) siderite are known from marine

54 mudstones and sandstones (e.g. Mozley and Carothers 1992; Mortimer et al. 1997; Wilkinson et al. 2000,

55 Weibel et al. 2010), whereas sphaerosiderite (with internal radial and/or concentric zonation) and spherulitic

56 siderite morphologies (with internal radial structures) and nodules/spheres of siderite (without clear internal

57 structures) are commonly of pedogenic origin (e.g. Browne and Kingston 1993; Retallack 1997; Driese et al.

58 2010; Robinson et al. 2010; Suarez et al. 2010; Rosenau et al. 2013) and are occasionally found in tidal flats

59 (Choi et al. 2003). A morphological change from spherulitic to rhombohedral siderite during diagenesis has

60 recently been suggested by Köhler et al. (2013) and renders the probability of other explanations for the

61 varying siderite morphologies. In a similar way to the changes during burial of marine sediments, the initial

62 microbial mediated fast precipitation may change into rhombohedral growth, as the supply of Fe becomes

63 slower during increased burial of continental deposits. Zonation is common in rhombohedral and spheroidal

64 siderite, and sphaerosiderites are characterized by internal radial-concentric microstructures. Siderite

65 zonation has previously been ascribed to mixing of meteoric and marine waters (Mozley 1989; Choi et al.

66 2003), diagenetic evolution of freshwater or brackish-marine pore water during burial (Matsumoto and Iijima

67 1981; Lim et al. 2004), or modification of the original marine pore waters during successive stages of

68 microbial decomposition of organic matter (Mozley and Carothers 1992; Wilkinson et al 2000; Lim et al.

69 2004). Despite the wide occurrence of sphaerosiderite, little is known of the pedogenetic conditions

70 (physical, chemical and biological) under which they form and when different siderite morphologies are

71 likely to precipitate (Driese et al. 2010). Precipitation of siderite, even within historical time (< 100 years)

72 shows that microbial degradation of organic contaminants can enhance siderite precipitation rate (Driese et

73 al. 2010). Hence, microbial activity in the pedogenic regime may have promoted precipitation of

74 sphaerosiderite. Siderite formation has been interpreted to be microbially mediated in various environments;

75 marine (Mozley and Carothers 1992; Wilkinson et al. 2000), tidal (Choi et al. 2003), and lacustrine (Fisher et

76   al. 1998). A wide range in carbon isotope composition ($\delta^{13}C$) of spharerosiderites is interpreted to originate

77   from variations in the type of microbial activity in soils (e.g. Robinson et al. 2010), whereas a more narrow

78   range of oxygen isotope compositions ($\delta^{18}O$) is thought to reflect meteoric water compositions (e.g., Ufnar et

79   al. 2004b; Driese et al. 2010; Robinson et al. 2010; Suarez et al. 2010). The latter has therefore been used as

80   a palaeoproxy for the isotope composition of rainfall, primarily during the Cretaceous (Ludvigson et al.

81   1998; Ufnar et al. 2001, 2002, 2004a, 2004b, 2004c; Suarez et al. 2009, 2010; Robinson et al. 2010).

82

83   The end-Triassic event is one of the five largest biotic crises during the Phanerozoic (Bond and Wignall

84   2014). It is temporally linked to the emplacement of intrusive and extrusive volcanic rocks during the

85   formation of the Central Atlantic Magmatic Province (Schoene et al. 2010; Blackburn et al. 2013), and

86   degassing from this volcanism is generally believed to have played a major part in the extinction scenario

87   (e.g., Hesselbo et al. 2002; Ruhl et al. 2011; Lindström et al. 2012). Organic $\delta^{13}C$ records across the

88   Triassic–Jurassic boundary show large negative perturbations in the carbon cycle interpreted as reflecting

89   input of light carbon from the volcanism or from methane release (e.g. Hesselbo et al. 2002). In the terrestrial

90   realm, physiological responses in fossil plants indicate intense global warming across the Triassic–Jurassic

91   boundary (McElwain et al. 1999). Increased storminess and lightning activity are further indicated by

92   charcoal records showing increased wildfire activity from Greenland, Denmark, Sweden and Poland

93   (Marynowski and Simoneit 2009; Belcher et al. 2010; Petersen and Lindström 2012). Sedimentary records

94   from the Danish Basin indicate increased reworking of palynological material (Lindström et al. 2012), and

95   marked changes in fluvial terrestrial successions in Sweden and Greenland seem to indicate an increased

96   water content in the hydrological cycle across the boundary (Lindström and Erlström 2006; Steinthorsdottir

97   et al. 2012).

98

99   Sphaerosiderites and other siderite morphologies have previously been reported from Triassic–Jurassic

100   boundary sediments (Höganäs Formation) in Scania, southern Sweden (Fig. 1; Troedsson 1951; Ahlberg

101   1994). Troedsson (1951) reported sphaerosiderites from early – middle Rheatian clayey sediments (Vallåkra

102   Member of the Höganäs Formation) in several old cored wells and outcrops in northwest and central Scania,

4

103   and concluded that sphaerosiderites were restricted to this particular interval. Here we show that

104   sphaerosiderites also occur within the latest Rhaetian sand and sandstones (Helsingborg Member of the

105   Höganäs Formation), although they are apparently absent from the intermediate part (Bjuv member of the

106   Höganäs Formation) (Fig. 1). The purpose of this study is to find explanations for the different siderite

107   morphologies and contribute to the understanding of sphaerosiderite formation, and its implications

108   regarding Triassic – Jurassic-boundary events. In northwest Scania, southern Sweden, the end-Triassic

109   terrestrial succession is characterized by a pronounced shift in depositional style and in occurrence of various

110   types of authigenic siderite. Mid to late Rhaetian forest mires and confined fluvial channel deposits are

111   completely free of authigenic siderite, whereas the overlying latest Rhaetian unconfined and probably

112   episodic braided river deposits are dominated by siderite concretions and authigenic siderite. In this sense,

113   the Albert-1 core, Norra Albert quarry and the Fleninge No. 266 core (Fig. 2), which together encompass

114   Norian–Hettangian strata, provide excellent opportunities for such investigations as perfectly zoned

115   sphaerosiderite occur juxtaposedwith other siderite morphologies.

116

117   *Fig. 1: Stratigraphy*

118

119   *Fig. 2: Map*

120

121

Geological setting

123

124   During the Late Triassic – Early Jurassic the Norwegian–Danish Basin was situated on the margin of an

125   epicontinental basin covering NW Europe (e.g. Fischer and Mudge 1998; Nielsen 2003). Southern Sweden

126   was part of the Fennoscandian Border Zone, which is structurally defined by the Sorgenfrei-Tornquist Zone,

127   and marks the transition from the Fennoscandian Shield to the north-east and the gradually deepening

128   (epicontinental) basin towards the south-west (Fig. 1; Liboriussen et al. 1987; Mogensen and Korstgård,

129   2003; Nielsen 2003). Therefore, minor sea-level changes played a significant role in controlling the lateral

130   facies distribution (Ahlberg et al. 2003). In Scania, the southernmost part of Sweden, typical continental red

131   beds of the Norian Kågeröd Formation, deposited under a semi-arid regime, are succeeded by claystones,

132   sandstones and coals belonging to the Rhaetian-Hettangian Höganäs Formation (Fig. 1). The oldest member

133   of the Höganäs Formation, the Vallåkra Member, consists of variegated smectitic clays and sands which

134   constitute a transition from the underlying red beds of the Kågeröd Formation to the kaolinite-rich

135   underclays, mature sands and coals of the Bjuv Member (Ahlberg et al. 2003). The Norwegian–Danish Basin

136   was transgressed in two steps (indicated on Fig. 1) during the Rhaetian, culminating with a maximum

137   transgression (MFS7) that can be traced all over the Danish part of the Norwegian–Danish Basin (Figs 1 and

138   3; Nielsen 2003; Lindström and Erlström 2006). The marine transgression reached as far in Scania as the

139   localities Helsingborg and Lunnom, and at Norra Albert an incursion of marine dinoflagellates probably

140   represents marine waters entering the rivers during storm episodes (Fig. 1; Lindström and Erlström 2006).

141   The precursor mires, resulting in the Bjuv Member coals/coaly beds, were formed on a low-relief coast

142   affected by a transgressive event in the mid-late Rhaetian (Petersen et al. 2013). The change from a semi-arid

143   climate during the Norian to more humid conditions during the Rhaetian has been attributed to effects of the

144   marine inundation of the Central European Basin from the Tethys (Ahlberg et al. 2002). Climatic changes at

145   the Triassic–Jurassic boundary that forced supraregional deforestation in NW Europe, (van de Schootbrugge

146   et al. 2009) which severely affected the forest mires (Petersen and Lindström 2012), may have triggered the

147   changes in continental deposits from mire forests and wetlands with confined fluvial channels (Bjuv

148   Member) to braided streams of the Boserup beds (Helsingborg Member) (Lindström et al. 2015). The

149   Boserup beds constitute the basal part of the Helsingborg Member (Sivhed 1984, Troedsson 1951). Some

150   authors have placed the boundary between the Bjuv Member and the Helsingborg Member at the top of coal

151   bed A, i.e. at c. 3 m in Fig. 3A (Sivhed 1984). In the Norra Albert quarry the boundary of the Boserup beds

152   has not been formally defined. In the present paper it is placed at 6 m in Fig. 3A based on sedimentological

153   considerations. The Bjuv Member is characterized by mudstones and coal beds with subordinate sandstones

154   interpreted as fluvial deposits. The overall depositional environment is interpreted as a floodplain. The coal

155   bed A is overlain by carbonaceous mudstone and with strongly deformed sand beds 5.0–6.2 m (Fig. 3A).

156   This succession comprises thin beds of fine-grained sand with graded bedding separated by mud-drapes. The

157   sand shows ripple-cross-lamination, indistinct lamination and locally parallel bedding. The sedimentary

158   structures suggest episodic, non-channelized deposition of sand in a flood-plain environment. Two phases of

159   soft-sediment deformations are interpreted caused by seismic shocks (Lindström et al. 2015). They are

160   erosionally overlain by the Boserup beds, which are a distinct association of facies dominated by structure

161   less, parallel bedded and trough cross-bedded sand, with several large concretions. The Boserup beds are

162   interpreted as braided stream deposits.

163

164   At the Norra Albert quarry and in the Fleninge No. 266 well this terrestrial ecosystem change is marked by a

165   gradual loss of Taxodiacean/Cupressacean gymnosperm pollen (*Perinopollenites elatoides*) from trees that

166   thrived in mires in favour of the enigmatic gymnosperm pollen tetrad *Ricciisporites tuberculatus*,

167   representing an unknown habit, perhaps ruderal / scrubby (Kürschner et al. 2014). A similar shift in

168   dominating pollen-type is recorded in marine sediments (the Stenlille-1 well – see Fig. 2) representing a

169   sediment source-area larger than that of the investigated terrestrial localities (Lindström et al. 2012). In

170   addition, repeated intervals of seismites occur at the Triassic-Jurassic transition at the Norra Albert quarry

171   (Lindström et al. 2015) coinciding with the occurrence of perfectly zoned sphaerosiderite (Fig. 2).

172

173   *Fig. 3: Sedimentary logs from Norra Albert quarry, Albert-1 and Fleninge No. 266 cores.*

174

175

176   **Methodology and terminology**

177

178   The samples comprise outcrop rock samples taken during field work in the Norra Albert quarry 2009 - 2012

179   and core samples from the Albert-1 and the Fleninge No. 266 wells, which were drilled in 2009 and 1935,

180   respectively. Consequently, the samples from the Fleninge No. 266 well were restricted by the limited

181   remaining core samples.

182

183   Petrography was evaluated from polished thin sections using a Zeiss Axioplane for transmitted and reflected

184   light microscopy. Supplementary studies of crystal morphologies, dissolution features and paragenetic

185   relationships were performed on gold coated rock chips mounted on stubs and on carbon coated thin sections

186   using a Phillips® XL 40 scanning electron microscope (SEM) operated with secondary electron detector

187   (SE) and back-scatter detector (BSE), respectively. The SEM was equipped with an energy dispersive X-ray

188   analysis (EDX) system Thermo Nanotrace® 30 mm^2 detector surface window and a Pioneer Voyager® 2.7

189   10 mm^2 window Si(Li) detector. The electron beam was generated by a tungsten filament operating at 17 kV

190   and 50-70 µA. One sample was partially dissolved in hydrochloric acid heated at 30°C in 2 hours under

191   agitation in order to enhance visibility of growth structures in the SEM.

192

193   Bulk samples for X-ray diffraction (XRD) analysis were mounted with random orientation. Samples were

194   scanned on an automated Philips® PW 3710 X-ray diffractometer with automatic divergence slit, using

195   graphite monochromated CuKα radiation. Quantification of major mineral phases based on bulk samples

196   was done by Rietveld analysis of X-ray diffractograms.

197

198   Total abundances of the major oxides and several minor elements were analysed by ICP-ES (inductively

199   coupled plasma-emission spectrometry) and the rare earth elements were determined by ICP-MS

200   (inductively coupled plasma-mass spectrometry) at ACME laboratory. The samples were fused by lithium

201   metaborate/ tetraborate and digested in dilute nitric acid. Total S and C were analysed by LECO. The major

202   elements were applied for calculation of mineral abundances.

203

204   Quantitative chemical analyses of the carbonates were performed on a JEOL® JXA-8200 electron

205   microprobe operated at an acceleration voltage of 15 kV, a beam current of 8 nA and a spot size of 10 µm.

206   Carbon coated thin section were applied.

207

208   Carbon and oxygen isotopes were analysed on bulk rock samples by IRMS (isotope ratio mass spectrometry)

209   and *in situ* by SIMS (secondary ion mass spectrometry) on thin sections. Bulk rock carbon and oxygen

210   isotope analyses using a VG SIRA II dual inlet mass spectrometer were performed on carbon dioxide

211   released from the carbonates after reaction with phosphoric acid at 25°C for 3 hours (calcites) and at 100°C

212   for 96 hours (siderites) at the SUERC facility in the UK. This way the major part of carbon dioxide produced

213   at 25°C will be from calcite, ensuring that the subsequent produced (at 100°C) carbon dioxide was

214   dominantly from siderite. The fractionation factors used were from Friedman and O'Neil (1977) (calcite) and

215   Rosenbaum and Sheppard (1986) (siderite). Carbon and oxygen isotope data ($\delta^{13}C$ and $\delta^{18}O$) are presented

216   in the standard δ notation relative to PDB, Pee Dee Belemnite (Craig 1957). In situ carbon and oxygen

217   isotopes measurements, were performed at the NORDSIM facility, Stockholm, using a CAMECA®

218   IMS1280 large-geometry ion microprobe using a 20 kV, ca. 10 μm Cs^+ primary beam, a low-energy

219   electron-flooding gun to compensate for charge build-up and simultaneous detection in either two Faraday

220   detectors (for ^{16}O and ^{18}O) or a Faraday together with an ion-counting electron multiplier (for ^{12}C and ^{13}C

221   respectively). All analyses were performed in automated chain sequences that regularly interspersed analyses

222   of unknowns with those of standards.   Because there is no universally accepted siderite standard we

223   developed our own through the Stable Isotope Facility (SIF) at the BGS using a VG Optima dual inlet mass

224   spectrometer and the Isotope Community Support Facility (ICSF) at SUERC using a VG SIRA II dual inlet

225   mass spectrometer). These two laboratories have slightly different analytical methods but agreed on the

226   preferred value for our principal standard, to which we compare our data. The siderite standard is from

227   Ivigtut cryolite deposits, Ivigttuut, Greenland. It was reacted under vacuum with anhydrous phosphoric acid

228   at a constant 100°C for 96 hours (SIF) and at 70°C for one week (ICSF). The CO_2 liberated was

229   cryogenically separated from water vapour under vacuum and analysed using IRMS. The mineral-gas

230   fractionation factor used for siderite was 1.00881 (derived from Rosenbaum and Sheppard, 1986). The

231   oxygen and carbon isotope composition of the siderite ($\delta^{18}O$ and $\delta^{13}C$) are reported as per mil (‰) deviations

232   of the isotope ratios ($^{18}O/^{16}O$ and $^{13}C/^{12}C$) calculated to the V-PDB scale. The SIF derived value for the

233   siderite standard was –21.97‰ (0.09 1SD) $\delta^{18}O$ and –8.08‰ (0.02 1SD) for $\delta^{13}C$. The ICSF derived value

234   for the siderite standard was –22.13‰ (0.23 1SD) $\delta^{18}O$ and –8.51‰ (0.17 1SD) for $\delta^{13}C$. Consequently,

235   average values of –22.04‰ (0.17 1SD) for $\delta^{18}O$ and –8.25‰ (0.24 1SD) for $\delta^{13}C$ were achieved when

236   compiling all standard measurements and were applied for correcting the SIMS data.

237

238

Results, sedimentology and petrography

240

Occurrence of siderite in the sediments

242

243   At the Norra Albert quarry siderite concretions are confined to the coarse-grained, poorly sorted, fluvial

244   sandstones of the Boserup beds and sporadic siderite cement in the uppermost part of the Bjuv Member (Fig.

245   3A), whereas their absence is notable in the underlying more clayey floodplain sediments of the Bjuv

246   Member. In general, the siderite concretions (ranging in size from 20 cm – 2 m) are developed preferentially

247   along the stratification (Fig. 4A, 4C and 4D). In some cases, the concretions appear to have initiated locally

248   in the most coarse-grained undulating intervals followed by continued siderite growth into the surrounding

249   finer-grained sand intervals, which cuts the sedimentary structures (Fig. 4E and 4F). In rare cases, petrified

250   wood occurs in the centre of siderite concretions (Fig. 4B).pure siderite occurs. The pure siderite can be

251   either detrital, very early siderite, or a late infilling in the centre of the concretion (cf. Bojanowski et al.

252   2016). Siderite may comprise a relatively large proportion of the concretions, suggesting that siderite

253   precipitation took place as displacive growth (Fig. 5).

254

255   The Albert-1 core (Fig. 3B) shows that authigenic siderite is absent in the Bjuv Member, though present in

256   the underlying Vallåkra Member. Core samples from the Fleninge No. 266 well (Fig. 3C) verify the presence

257   of perfectly zoned sphaerosiderite and other authigenic siderite morphologies in the lower part of the

258   Boserup beds; and confirm that authigenic siderite is absent in the Bjuv Member, though present at the

259   boundary to Vallåkra Member (Fig. 3C).

260

261   *Fig. 4: Siderite concretions at N Albert quarry*

262

263   *Fig. 5: Calculated mineral abundance*

264

265

Siderite micromorphology

267   The siderite micromorphologies are divided into the following types that precipitated in successive order:

268   1. Zoned sphaerosiderite and spheroidal siderite, which is subdivided into: 1A perfectly zoned

269   sphaerosiderite: 1B poorly zoned sphaerosiderite (and spherulites); and 1C zoned spheroidal siderite.

270   2. Radial siderite overgrowths, which exhibit variable habits according to their substratum: from

271   mainly rhombohedral on the perfectly zoned sphaerosiderite (A) to preferentially fibrous, when

272   growing on the spheroidal siderite (B).

273   3. Microcrystalline, anhedral or subhedral, randomly orientated pervasive siderite cement that forms

274   concretionary cements. Rhombohedral single siderite crystals dispersed in the sandstones are

275   considered initial precipitations in 'immature concretions' (compare with Bojanowski et al. 2016).

276

Zoned sphaerosiderite and spheroidal siderite

278   Perfectly zoned sphaerosiderite and zoned spheroidal siderite are common in the siderite concretions in a

279   specific interval in the Boserup beds partly coincident with the interval of soft sediment deformation

280   structures (Fig. 3A). Poorly zoned sphaerosiderite generally occurs scattered, though is occasionally

281   abundant in concretions, immediately below this interval, i.e. in the uppermost part of the Bjuv Member (Fig.

282   3A and 3C). Scattered poorly zoned sphaerosiderites are common in concretions in the overlying Boserup

283   beds (Fig. 3A). Poorly zoned sphaerosiderite occurring in the basal part of the Bjuv Member (Fig. 3C) never

284   encloses detrital grains and are oversized compared with sphaerosiderite in the Bjuv and Helsingborg

285   members, though similar to those occurring in the Vallåkra Member analysed by Troedsson (1951) and

286   slightly resembling the cemented areas of the Vallåkra Member in the Albert-1 well (AL1-09.28 in Fig. 3B).

287   These oversized sphaerosiderite may not have been formed *in situ* within the Bjuv Member deposits, but

288   probably precipitated in older strata (e.g. Vallakra Member) and were redeposited.

289

290   Poorly zoned sphaerosiderite has an inner core surrounded by a rim of rhombohedral or irregular crystals

291   (Fig. 6). Perfectly zoned sphaerosiderite has an inner core of radiating growth (which gives rise to a

292   characteristic extinction pattern) in few to several concentric zones (Fig. 7). The outermost rim of

293   rhombohedral crystals is partly coalescent with the cement filling the shrinkage fracture between the detrital

294   grains and sphaerosiderite. Sphaerosiderite commonly occurs in clusters (Figs 7E and 8B) forming a coccoid

295   morphology (compare Driese et al. 2010). Sphaerosiderite zonation is caused by variation in mineralogy and

296   chemistry. Rhodochrosite zones in sphaerosiderite seem to be more affected by dissolution than siderite (Fig.

297   8A). Rhodorchrosite abundance of up to 25% of the cement of one concretion is documented by XRD. In

298   other concretions, ankerite dolomite and/or rhodochrosite are occasionally present in XRD detectable

299   amounts. Poorly zoned sphaerosiderite occur with dissolution voids next to poorly zoned sphaerosiderite

300   having a core of increased Ca, Mn and Si contents, suggesting that dissolution preferentially occurred in

301   other carbonate phases and low Fe siderite (Fig. 6B and 6D). Zonation enhanced by weathering in other

302   sphaerosiderites (Fig. 7C) may also originate from other carbonate minerals or incorporation of varying

303   amounts of Ca, Mn (Mg?) and Zn in the siderite structure (Fig. 8A and 8C). Zonation patterns are uniform

304   within concretions, though vary between different concretions (Figs 7D and 8A).

305

306   Zoned spheroidal siderite has an inner core of radiating crystals similar to the perfectly zoned

307   sphaerosiderite, and only few but regular spheroidal zones (Fig. 9). The spheroidal siderite has a more

308   uniform size (30 – 80 μm) than the size of the perfectly zoned sphaerosiderite (20 – 350 μm) and the usual

309   size of poorly zoned sphaerosiderite (3 – 170 μm) (Fig. 3).

310

311

312

Overgrowths on siderite morphologies

Perfectly zoned sphaerosiderite is typically surrounded by a rim of rhombohedral siderite crystals (Fig. 7).The outermost rim of rhombohedral crystals is partly coalescent with fracture-healing cement between the detrital grains and perfectly zoned sphaerosiderite (Fig. 7A, 7B and 7D). The overgrowths on the zoned spheroidal siderite preferentially consist of radiating crystals (Fig. 9A).

Concretionary siderite cement

Sparry, microspar or micritic siderite cement encloses perfectly and poorly zoned sphaerosiderite and spheroidal siderite to form concretions. Dispersed rhombohedral siderite and poorly zoned sphaerosiderite characterise the weakly-cemented sandstones in the lower part of the exposed Boserup beds at Norra Albert, whereas the upper exposed part of the Boserup beds have concretions with poorly zoned sphaerosiderite (Fig. 3A). The dispersed siderite occurs preferentially in the most coarse-grained intervals.

Siderite in relation to other minerals

Siderite is typically non-corrosive against detrital grains, which support a displacive growth of the siderite cement. However, siderite crystals and spheres grow along cleavage planes in mica and feldspar and more rarely in secondary porosity after feldspar and altered Fe-Ti oxides. Few authigenic phases predate siderite. Rare pyrite, enclosing micro-spheres of siderite, is enclosed in the centre of sphaerosiderite so pyrite mainly predates siderite. Kaolinite (crystal sizes: 2 – 4 µm) occur enclosed in rhombohedral siderite and partly dissolved feldspar, and are enclosed in sparry siderite cement. Other authigenic phases, such as kaolinite (crystal size: 5 – 10 µm), anatase and possibly quartz, occur in the central dissolution voids after poorly zoned sphaerosiderite (Fig. 6C) and consequently postdate siderite. The authigenic origin of quartz is suggested from its euhedral shape and from the ubiquitous initial quartz overgrowths on detrital quartz, in general.

13

339

340   Alteration products, such as manganese oxides/hydroxides and iron-oxides/hydroxides, are common in most

341   sandstones. Iron-oxide/hydroxides (hematite in one sample) occur in altered zones of sphaerosiderite and

342   spheroidal siderite and as alteration rims around rhombohedral siderite. Manganese oxides/hydroxides occur

343   as authigenic rims around detrital and authigenic phases, though without any specific petrographic

344   relationship to the chemistry of the carbonate phases.

345

346   *Fig. 6: Poorly zoned sphaerosiderites (spherulites, spherulitic siderite)*

347

348   *Fig. 7: Perfectly zoned sphaerosiderites*

349

350   *Fig. 8: Varieties of zoned sphaerosiderites*

351

352   *Fig. 9: Spheroidal siderite (pseudomorphs after organic matter?)*

353

Chemical composition

355   Low CaMg siderites (Fig. 8) dominate all siderite morphologies with typically < 5 % $CaCO_3$ and < 3 %

356   $MgCO_3$. Maximum 11 % $MgCO_3$ (sample 516816), 10 % $CaCO_3$ (sample 516814) and up to 0.9 % $ZnCO_3$

357   occur in some samples. $MnCO_3$ is more common with up to 10 %. Poorly zoned sphaerosiderite has a

358   tendency of slightly higher content of $CaCO_3$, up to 10 %, than other siderite micromorphologies. Zoned

359   spheroidal siderite, perfectly zoned sphaerosiderite and their overgrowths have the highest content of

360   $MnCO_3$, up to 35 % (Fig. 8).

361

362   *Fig. 10: Chemical composition*

363

364 **Isotope composition**

365 The $\delta^{18}O$ of siderite is mostly unrelated to the siderite morphology, because concretions and weakly

366 cemented sandstones containing perfectly zoned and poorly zoned sphaerosiderite, spheroidal and

367 rhombohedral siderites appear with similar oxygen isotopic compositions (SIMS: –4.7 to –5.1‰ $\delta^{18}O$ and

368 IRMS:–4.8 to –5.3‰ $\delta^{18}O$) (Table 1; Fig. 11). Sphaerosiderite with rhodochrosite zones group together with

369 other perfectly zoned sphaerosiderites (Fig. 11A). Samples containing small rhombohedral siderites, which

370 are more prone to alteration, have relatively lower $\delta^{18}O$ values (down to –7.5‰). One intensively altered

371 sample with even lower values has been left out, as the high amounts of iron-oxide/hydroxides affected the

372 oxygen isotopic composition.

373

374 The SIMS measurements show clearly more positive $\delta^{13}C$ values for the concretionary cement (–5.5 to

375 +7.8‰) than for the siderite micromorphologies, such as perfectly zoned sphareosiderite (–17.3 to –2.4‰),

376 spheroidal siderite (–101.1 to –5.1‰) and their overgrowths (–13.0 to +3.0‰) (Fig. 11B). The somewhat

377 wider span in $\delta^{13}C$ values (–17.3 to +7.8‰) for the *in situ* SIMS measurements compared to bulk rock IRMS

378 measurements (–11.6 to +6.0‰ $\delta^{13}C$) is a result of different mixtures of sphaerosiderite and spheroids and

379 concretionary cement in the bulk rock samples.

380

381 *Fig. 11: Isotopic composition*

382

383 *Table 1. Isotopic composition*

384

385

386

387

388

389 # Discussion

390

391 ## Microstructural growth pattern

392

393 A wide spectrum of siderite morphologies is represented in the Norra Albert quarry. It is remarkable to find

394 perfectly concentrically-zoned sphaerosiderite, spheroidal siderite, rhombohedral siderite and poorly-zoned

395 sphaerosiderite occurring together. Poorly zoned sphaerosiderite could be the precursor to perfectly zoned

396 sphaerosiderite, which forms only under specific conditions.

397

398 Poorly-zoned sphaerosiderite and spherulites with central dissolution voids cannot, strictly speaking, be

399 distinguished. Internal dissolution voids in rhombohedral siderite and spherulites may origin from siderite

400 growths around a core of different chemistry or carbonate mineralogy, an episode of crystal poisoning

401 (Wilkinson et al. 2000) or it may be explained by areas ('eyes') of less stability within the spherulites

402 originating from its primary growth pattern (Gránásy et al. 2005). In the latter case no chemical or

403 mineralogical zonation is necessary in order to explain the central instability.

404

405 Radiating growth patterns are characteristic of the centre of perfectly zoned sphaerosiderite and spheroidal

406 siderite (Figs 7 and 9), but are more difficult to discern within the spherulites and poorly zoned

407 sphaerosiderites. The growth begins from a nucleus that seems very small in the sphaerosiderite. The

408 constrained spheroidal shape suggests some kind of growth control, possibly of organic origin, for example

409 within spheroidal pollen grains or within stomata of leaf cuticles (compare stomata of leafs of *ginkgoites* or

410 *anomozamites* known from a Rhaetian flora in Scania reported by Pott and McLoughlin (2011)). Siderite

411 precipitation may have started along the inside of the pollen wall as the spore-cell material decayed, or along

412 the guard cells of the open pores of the stomata, with subsequent continued growth inwards towards the

413 centre of the pollen grain/ stomata. As the organic matter degraded, growth of siderite radiating outwards

414 from the original location of the guard cells followed. Other types of organic matter may have acted as

415   nucleation sites for the sphaerosiderite growth. The growth pattern changes from radial to rhombohedral, as

416   spherulites were enclosed in sparry or rhombohedral siderite, and as rhombohedral crystals rimmed the

417   perfectly zoned sphaerosiderite (Fig. 7C and 7D). This change in growth pattern could reflect biogenically

418   facilitated, radially- and concentrically-zoned siderite, succeeded by a relatively slower precipitation of

419   siderite, beginning with rhombohedral crystals and ending with sparry and/or microsparry cement. A

420   diagenetically-induced change of spherulitic to rhombohedral siderite morphology is advocated by Köhler et

421   al. (2013), but it seems less likely that only the outermost part of the sphaerosiderite and spherulites should

422   be diagenetically altered prior to enclosure in sparry or microsparry siderite cement. In this case, a more

423   reasonable explanation would be continued growth under changed conditions and hence with different

424   precipitation rates, from bacterially-mediated Fe^{3+} reduction to microbial fermentation of organic matter in

425   the methanogenic zone (e.g. Hicks et al. 1996; Ludvigson et al. 1998; Krajewski et al. 2010).

426

427   The perfect zonation of sphaerosiderite is so pronounced and systematic (Fig. 7D) that it cannot merely have

428   formed from alteration processes. Rather, the alteration processes have enhanced the visibility of the detailed

429   zonation (Fig. 8A) with *in situ* alteration products of iron-oxide/hydroxide and dissolution voids after less

430   stable phases such as Ca or Mn-rich siderite and rhodochrosite. Dissolution voids begin within the pure

431   rhodochrosite zones rather than in the siderite, so rhodochrosite zones dissolve faster than siderite (Fig. 9A).

432   Rhodochrosite forms under suboxic conditions whereas siderite precipitates under anoxic conditions

433   (Bojanowski et al. 2016), hence rhodochrosite is likely to be more stable under oxidizing conditions.

434   However, dissolution products of rhodochrosite are removed faster from points of dissolution since Mn^{2+} is

435   slightly more soluble than Fe^{2+} (Sholkovitz and Copland 1981). The central part of the spherulites and

436   poorly zoned sphaerosiderites is commonly dissolved; but when present the central part generally has higher

437   contents of Mn, Ca, and occasionally Si. It is therefore probable that the dissolution zones/centres are located

438   where the siderite has incorporated relatively high amounts of Mn and Ca. This would explain the common

439   occurrence of *ex situ* manganese-oxides/hydroxides as alteration rims covering both detrital grains and

440   authigenic phases, though without any petrographic association with siderite or rhodochrosite.

Bacterial mediated perfect zonation?

The growth of sphaerosiderite started on organic or detrital grains and continued in spherical zones around the nuclei as the bacterial colony continued its reduction of Fe and Mn, which reacted with HCO_3^-, liberated from the degradation of organic matter and precipitated as siderite (and rhodochrosite). Spheroidal siderite started as impregnation of voids in organic tissue, for example pollen or stomata, and continued with zonal growth of siderite crystals on the pollen wall or the guard cells and gradually filled the void (Fig. 12). This could explain the uniform size of spheroidal siderite (Fig. 4A). After degradation of the surrounding organic matter, the siderite growth continued outwards with larger radiating crystals, possibly reflecting more slowly sourced iron.

Most investigations of sphaerosiderite record large variations in $\delta^{13}C$ (Table 1; e.g. Ludvigson et al. 1998; Driese et al. 2010; Robinson et al. 2010; Suarez et al. 2010). The range in $\delta^{13}C$ values of sphaerosiderite and spheroidal siderite, in general, and in this investigation, is large (–17.3 to –2.4‰ for sphaerosiderite and –10.1 to –5.1 ‰ for spheroidal siderite) (Table 1; Fig. 11). This may reflect either a variety in the microbes (bacteria and fermenters), which produced CO_2 / HCO_3^- for siderite precipitation, or it could represent a mixture of two different end-members of bicarbonate. Bicarbonate from the decomposition of organic matter in the suboxic zone represents the low $\delta^{13}C$ values of sphaerosiderite and spheroidal s, whereas bicarbonate originating from methanogenic fermentation of organic matter is responsible for the relatively high $\delta^{13}C$ values of the concretionary cement (Fig. 11; e.g. Irwin et al. 1977; Mozley and Wersin 1992; Ludvigson et al. 1998; Krajewski et al. 2010). The shift in $\delta^{13}C$ values (Fig. 11) is accompanied by a change in crystal morphology from radiating growth in sphaerosiderite to rhombohedral overgrowths and cement (Figs 7), which also may be explained by a shift from bacterially-mediated growth in the iron reduction zone to precipitation in the methanogenic zone.

466   The zonation within the perfectly zoned sphaerosiderites is caused by variation in carbonate mineralogy and

467   chemistry, and reflects availability of Fe, Mn, Ca and Mg in the neighboring/local environment. The rate of

468   iron reduction, and hence the availability of Fe^{2+}, is the limiting factor on precipitation of microbial siderite

469   (Mortimer et al. 1997). In addition to Fe, Mn, Mg, Zn and Ca abundance in the fluids, variation in nutritional

470   stress and physical conditions, for example temperature, also influence the iron reduction rate and hence the

471   incorporation of other elements, like Mn (Mortimer et al. 1997). Coccoid morphology/clusters of

472   sphaerosiderite and areas of sphaerosiderite with identical zonation pattern (Figs 7E and 8A) probably mark

473   the outline of microbial communities. The zonation pattern within one microbial community may represent

474   minor episodes of drying-out or harsh/hostile conditions for the microbes. During such dry periods,

475   shrinkage, partial dissolution and alteration of the protruding outgrowths may ensure its spherical/rounded

476   shape (Fig. 12).

477

478

479   **Microscale variations reflecting groundwater fluctuations**

480

481   Causes of zonation can be divided into two general explanations/hypotheses: 1) mixing of meteoric and

482   marine waters (Mozley 1989; Choi et al. 2003) and 2) modification of the original pore waters during

483   successive stages of microbial decomposition of organic matter (Mozley and Carothers 1992; Lim et al.

484   2004). The latter is almost identical to the explanation by Wilkinson et al. (2000) that siderite precipitation

485   takes place during gradual burial within the Fe and Mn reduction zones, while dissolution takes place in the

486   sulphate reduction zone, and siderite growth in the methanogenic zone.

487   The siderite morphologies found in the Boserup beds at Norra Albert provide two important contributions to

488   this dispute on the origin of zonation due to their microscale and macroscale variations in morphology and

489   stable isotope geochemistry. The observed microscale variations in siderite zonation pattern in the

490   sphaerosiderites (Figs 7A, 7E, 8A, 8C) cannot be explained by either of the hypotheses described previously.

491   Though marine excursions may have occurred in the Boserup beds during storm episodes, similar to the

492 marine occurrences in the Bjuv Member at other localities in Scania (Lindström and Erlström 2006), marine

493 influxes in a meteoric-dominated environment ought to have affected all sphaerosiderites. The chemical

494 composition is typically low in Mg and Ca for all siderite micromorphologies (Fig. 10), which suggests

495 meteoric water composition (Matsumoto and Iijima 1981; Mozley 1989; Browne and Kingston 1993). Pyrite

496 occurs rarely, and when present as a very early phase enclosed in the centre of the sphaerosiderite. This

497 indicates that sulphate was limited from the time of deposition and that iron reduction took over instead of

498 sulphate reduction. Furthermore, the $\delta^{18}O$ values in all siderite morphologies from Norra Albert are very

499 consistent, close to the meteoric water composition, and show no influence from marine water (Fig. 11).

500

501 If the zonation pattern reflects depth-controlled burial processes (as suggested by Mozley and Carothers

502 1992; Wilkinson et al. 2000), then repeated small tectonic movements or variations in sedimentation

503 rate/erosion would be required to explain the numerous changes through the Fe-reduction, Mn-reduction,

504 sulphate reduction and methanogenic zones. These possibilities seem unlikely as the fluvial style of the

505 Boserup beds does not change over this interval. Groundwater fluctuations seem a more likely explanation

506 and are supported by additional features besides the perfectly zoned sphaerosiderite. Siderite cementation in

507 shrinkage-fractures between detrital grains and sphaerosiderite could either be a result of mechanical

508 compaction or caused by a period of shrinkage occurring during drying-out, either due to subaerial exposure

509 or to lowering of the water table before siderite was again precipitated in the shrinkage fractures (Figs 7A,

510 12). The possibility that it could have been caused by mechanical compaction seems less likely, since

511 fractured sphaerosiderites only occur in one concretion. Fluctuations in groundwater table would result in

512 multiple changes in the physiochemical condition and the microbial life conditions. A longer growth period

513 could explain the numerous zones and the necessity of using other metals, e.g. Mn and Zn, as the Fe source

514 for the bacterial metabolism was exhausted. The presence of hematite suggests that siderite precipitation

515 was followed by its alteration to iron-oxide/hydroxides in the unsaturated zone prior to burial diagenesis, as

516 hematite replaced iron-oxide/hydroxides (not siderite) either due to aging (Van Houten 1961), which is less

517 likely in Triassic – Jurassic sediments, or at enhanced temperatures (> 56°C) (Weibel 1999). The Triassic–

518 Jurassic-boundary strata in Scania have been subjected to moderate burial temperatures < 85°C (inferred

519 from vitrinite reflectance by Ahlberg 1994) and > 65°C (due to restricted quartz diagenesis, in comparison

520 with Weibel et al. 2010). Hence, fluctuations in groundwater level during deposition of the Boserup beds is

521 the most plausible explanation for both sphaerosiderites with numerous zones of slightly varying

522 composition, formation of hematite, and healing shrinkage cracks.

523

524 As elsewhere in NW Europe, the Danish part of the Norwegian–Danish Basin was subjected to major sea-

525 level changes at this time, the "regression–transgression couplet" that may have been linked to tectonic

526 movements during the formation of the Central Atlantic Magmatic Province (Hallam 1997; Hallam and

527 Wignall 1999). The underlying Bjuv member is interpreted to have been deposited during a transgression

528 and as part of a highstand systems tract (Petersen et al. 2013), with the maximum flooding surface MFS7 of

529 Nielsen (2003) situated between coal seams B and A, whereas the Boserup beds, in contrast, were formed

530 during a lowstand systems tract. However, these sea-level changes would not necessarily have caused

531 repeated fluctuations in groundwater level during the deposition of the Boserup beds. The high proportion of

532 structure less sandstones in the Boserup beds suggests rapid deposition, possibly from flash floods, rather

533 than through bedform migration, and associated liquefaction/fluidization processes. A more extreme climate

534 with increased humidity and storminess in the late Rhaetian (Petersen and Lindström 2012), strong

535 seasonality with episodic storms of heavy rain, alternating with periods of enhanced drought, could be

536 responsible for a fluctuating groundwater table. The co-occurrence of humid habitats and floral elements

537 with xeromorphic features, i.e. features that may be linked to physiological drought, in the Rhaetian flora in

538 Scania (Pott and McLoughlin 2011) may possibly also be ascribed to groundwater fluctuations or seasonal

539 drought. There is also the possibility that the fluctuations in ground-water table were linked to increased

540 repeated seismicity during this time (Lindström et al. 2015), because changes in groundwater levels are a

541 common effect during earthquakes (Wang and Manga 2010). The perfectly zoned sphaerosiderites occur in

542 the upper part of soft-sediment deformation structures – "seismites"– identified at both Norra Albert and in

543 the Fleninge No. 266 core (Figs. 3A and C). Soft- sediment deformation structures form in unconsolidated,

544 water-saturated sediments (e.g. Topal and Özkul 2014), and hence are likely to have formed close to the

545 groundwater table. Fracturing and displacement of sphaerosiderite, followed by fracture healing (Fig. 7D),

21

546 show that local deformation occurred shortly after early diagenesis and could be related to mechanical

547 compaction or soft-sediment deformation structures triggered by seismic events (Lindström et al. 2015).

548

549

550 **Conclusions**

551

552 The late Rhaetian terrestrial succession in northwestern Scania exhibits a variety of siderite

553 micromorphologies, comprising perfectly zoned sphaerosiderite, poorly zoned sphaerosiderite (possibly

554 identical with spherulitic siderite), spheroidal siderite and their rhombohedral and fibrous siderite

555 overgrowths, enclosed in sparry, microspar and micritic concretionary siderite cement. The siderite formed

556 in an apparently similar early diagenetic/pedogenic environment, as indicated by similar trace element

557 variations and meteoric water oxygen isotopic compositions. The characteristic broad range in carbon

558 isotopic compositions indicates that different microbes in the pedogenic environment were involved in

559 degradation of organic matter and supplied C for siderite formation. Here the carbon isotopic composition

560 can be subdivided into sphaerosiderite and spheroidal siderite of low values (-17.3 to -2.4‰ δ^{13}C) and their

561 rhombohedral or fibrous siderite overgrowths of almost similar values (-13.0 to $+3.1$‰ δ^{13}C) sourced from

562 bacterial degradation of organic matter in the Fe-reduction zone. This was followed by concretionary siderite

563 cement of higher isotopic values (-5.8 to $+7.8$‰ δ^{13}C) promoted by fermentation activity in the

564 methanogenic zone. Growths of spheroidal siderite may have initiated on organic compounds, for example

565 palynomorphs or stomata; likewise sphaerosiderite growth probably started on other, but specific, types of

566 organic matter, which served as a microbial energy source and controlled the initial crystal growth.

567

568 Perfectly-zoned sphaerosiderite is restricted to the Boserup beds. The perfect multi-layered zonation is

569 related to heterogeneous alteration caused by mineralogical and geochemical variations. The zonation

570 reflects microbial activity, their life conditions, and availability of Fe, Mn, Ca and other cations in the pore

571 water. These conditions are linked to amount of precipitation, water flow and groundwater-level fluctuations.

572   Intervals of continuous water-saturation and flow through the sediments resulted in Fe-rich siderite

573   precipitation in the Fe-reduction zone. Under unsaturated or poorly saturated conditions, for example during

574   episodes of lowered water table, rhodochrosite and Mn-rich siderite formed when the microbial community

575   experienced hostile life conditions and/or the Fe supply was exhausted. The change from the saturated to

576   unsaturated zone caused partial dissolution of poorly and perfectly zoned sphaerosiderite, which explains

577   their continued spherical zonation and rounded shape. The inferred changes in groundwater level suggest

578   deposition under a strongly seasonal climate with episodic drought. During burial the siderite precipitation

579   style changed from bacterially mediated spherical and radiating growth in the Fe-reduction zone to

580   rhombohedral precipitation in the methanogenic zone and still characterized by meteoric water of $-5.1‰$

581    $\delta^{18}O$ at a c. 45°N latitudinal position of Scania.

582

583

584 **Acknowledgments**

585

593

594

References

595

596 Ahlberg, A. 1994. Deposition and diagenesis of the Rhaetian-Hettangian succession (Triassic-Jurassic) in

597 southern Sweden: a synthesis. Lund Publication in Geology No. 123, 137p.

598 Ahlberg, A., Arndorff, L., Guy-Ohlson, D. 2002. Onshore climate change during the Late Triassic marine

599 inundation of the Central European Basin. Terra Nova 14, 241–248.

600 Ahlberg, A., Olsson, I. and Šimkevičius, P. 2003.Triassic–Jurassic weathering and clay minerals dispersal in

601 basement areas and sedimentary basins of southern Sweden. Sedimentary Geology 161, 15–29.

602 Anderson, T. F., Arthur, M. A. 1983. Stable isotopes of oxygen and carbon and their application to

603 sedimentologic and palaeoenvironmental problems. In: Arthur, M. A., Anderson, T. F., Kaplan, I. R., Veizer,

604 J., Land, L. S. (Eds.). Stable isotopes in sedimentary geology. SEPM course No. 10, Dallas 1983, 1-1–1-151.

605 Andrews, L. L. 2014.The Jurassic shales of the Weald Basin: geology and shale oil and shale gas resource

606 estimation. Appendix G. British Geological Survey for Department of Energy and Climate Change, London,

607 UK, 79p.

608 Baker, J. C., Kassan, J., Hamilton, P. J. 1996. Early diagenetic siderite as an indicator of depositional

609 environment in the Triassic Rewan Group, southern Bowen Basin, eastern Australia. Sedimentology 43, 77–

610 88.

611 Belcher, C.M., Mander, L., Rein, G., Jervis, F.X., Haworth, M., Hesselbo, S.P., Glasspool, I.J., McElwain,

612 J.C. 2010. Increased fire activity at the Triassic/Jurassic boundary in Greenland due to climate-driven floral

613 change. Nature Geoscience 3, 426–429.

614 Blachburn, T. J., Olsen, P. E., Bowring, S. A., McLean, N. M., Kent, D. V., Puffer, J., MacHone, G.,

615 Rasbury, E. T., Et-Touham, M. 2013. Zircon U-Pb geochronology links the end-Triassic extinction with the

616 Central Atlantic Magmatic Province. Science 340, 941–945.

617   Blakey, R. 2016. Palaeomaps (http://cpgeosystems.com/paleomaps.html)

618   Bond, D. P. G. and Wignall, P. B. 2014. Large igneous provinces and mass extinctions: An update.

619   Geological Society of America Special Publication 505, 29–56.

620   Bojanowski, M. J., Jaroszewicz, E., Košir, A., Łoziński, M., Marynowski, L., Wysocka, A., Derkowski, A.

621   2016. Root-related rhodochrosite and concretionary siderite formation in oxygen-deficient conditions

622   induced by a ground-water table rise. Sedimentology 63, 523 – 551.

623   Browne, G. H, Kingston, D. M. 1993. Early diagenetic spherulitic siderites from Pennsylvanian palaeosols in

624   the Boss Point Formation, Maritime Canada. Sedimentology 40, 467–474.

625   Carothers, W. W., Adami, L. H., Rosenbauer, R. J. 1988. Experimental oxygen isotope fractionation between

626   siderite-water and phosphoric acid liberated CO_2-siderite. Geochimica et Cosmochimica Acta 52, 2445– 450.

627   Choi, K. S., Khim, B. K. & Woo, K. S. 2003. Spherulitic siderites in the Holocene coastal deposits of Korea

628   (eastern Yellow Sea). Elemental and isotopic composition and depositional environment. Marine Geology 202,

629   17–31.

630   Cleveland, D.M., Nordt, L.C., Dworkin, S.I., Atchley, S.C. 2008. Pedogenic carbonate isotopes as evidence

631   for extreme climatic events preceding the Triassic–Jurassic boundary: Implications for the biotic crisis.

632   Geological Society of America Bulletin 120, 1408–1415.

633   Craig, H. 1957. Isotopic standards for carbon and oxygen correction factors for mass spectrometric analysis

634   of carbon dioxide. Geochimica et Cosmochimica Acta 12, 133–149.

635   Driese, S. G., Ludvigson, G. A., Roberts, J. A., Fowle, D. A., González, Smith, J. J., Vulava, V. M., McKay,

636   L. D. 2010. Micromorphology and stable-isotope geochemistry of historical pedogenic siderite formed in

637   PAH contaminated alluvial clay soils, Tennessee, U.S.A. Journal of Sedimentary Research 80, 943–954.

638   Friedman, I., O'Neil, J. R. 1977. Compilation of stable isotopic fractionation factors of geochemical interest.

639   US Geological Survey Prof. Paper 440-KK, 12 pp.

640   Fischer, M. J., Mudge, D. C. 1998. Triassic. In: Glennie, K. W. (Ed.) Petroleum geology in the North Sea –

641   Basic concepts and recent advances 4th edition. Blackwell Sciences, 212–244.

642   Fisher, Q. J., Raiswell, R., Marshall. J. D. 1998. Siderite concretions from nonmarine shales (Westphalian A)

643   of the Pennines England: Controls on their growth and composition. Journal of Sedimentary Research 68,

644   1034–1045.

645   Fritz, P., Binda, P. L., Folinsbee, F. E., Krouse, H. R. 1971. Isotopic composition of diagenetic siderites from

646   Cretaceous sediments in Western Canada. Journal of Sedimentary Petrology 41, 282–288.

647   Gránásy, L., Pusztai, T., Tegze, G., Warren, J. A., Douglas, J. F. 2005. Growth and form of spherulites.

648   Physical Review E 72, 011605-1 – 011605-15.

649   Hallam, A. 1997. Estimates of the amount and rate of sea-level change across the Rhaetian–Hettangian and

650   Pliensbachian–Toarcian boundaries (latest Triassic to early Jurassic). J. Geol. Soc. London 154, 773–779.

651   Hallam, A., Wignall, P.B. 1999. Mass extinctions and sea-level changes. Earth-Science Reviews 48, 217–

652   250.

653   Hesselbo, S. P., Robinson, S. A., Surlyk, F., Piasecki, S. 2002. Terrestrial and marine extinction at the

654   Triassic-Jurassic boundary synchronized with a major carbon-cycle perturbation: A link to initiation of

655   massive volcanism? Geology 30, 251–254.

656   Irwin, H., Curtis, C. D., Coleman, M., 1977. Isotopic evidence for source of diagenetic carbonates formed

657   during burial of organic-rich sediments. Nature 269, 209–213.

658 Krajewski, K. P., Gonzhurov, N. A., Laiba, A.A., Tatur, A. 2010. Early diagenetic siderite in the Panorama

659 Point Beds (Radok Conglomerate, Early to Middle Permeian), Prince Charles Mountains, East Antarctica.

660 Polish Polar Research 31, 169–194.

661 Köhler, I., Konhauser, K. O, Papineau, D., Bekker, A., Kappler, A. 2013. Biological carbon precusor to

662 diagenetic siderite with spherical structrues in iron formations. Nature Communication 4:1741 DOI:

663 10.1038/ncomms 2770.

664 Liboriussen, J., Ashton, P., Thygesen, T. 1987. The tectonic evolution of the Fennoscandian Border Zone in

665 Denmark. In: Ziegler, P. A. (ed.), Compressional intra-plate deformations in the Alpine Foreland.

666 Tectonophysics 137, 21–29.

667 Lim, D. I., Jung, H. S, Yang, S. Y., Yoo, H. S. 2004. Sequential growth of early diagenetic freshwater

668 siderites in the Holocene coastal deposits, Korea. Sedimentary Geology 169, 107–120.

669 Lindström S., Erlström, M. 2006. The late Rhaetian transgression in southern Sweden: Regional (and global)

670 recognition and relation to the Triassic – Jurassic boundary. Palaeogeography, Palaeoclimatology,

671 Palaeoecology 241, 339–372.

672 Lindström, S., van de Schootbrugge, B., Dybkjær, K., Pedersen, G. K., Fiebig, J., Nielsen, L. H., Richoz, S.

673 2012. No causal link between terrestrial ecosystem change and methane release during the end-Triassic mass

674 extinction. Geology 40, 531–534.

675 Lindström, S., Pedersen, G. K., van de Schootbrugge, B., Hansen, K. H., Kuhlmann, N., Thein, J.,Johansson,

676 L., Petersen, H. I., Alwmark, C., Dybkjær, K., Weibel, R., Erlström, M., Nielsen, L. H.. Oschmann, W.,

677 Tegner, C. 2015. Intense and widespread seismicity during the end-Triassic mass extinction due to

678 emplacement of a large igneous province. Geology 43, 387–390.

679   Lund, J. J. 1977. Rhaetic to Lower Liassic palynology of the onshore south-eastern North Sea Basin.

680   Geological Survey of Denmark II Series, 109, 105p.

681   Ludvigson, G. A., González, L. A., Mtzger, R. A., Witzke, B. J., Brenner, R. L., Murillo, A. P., White, T. S.

682   1998. Meteoric sphaerosiderite lines and their use for paleohydrology and paleoclimatology. Geology 26,

683   1039–1042.

684   Marynowski, L., Simonet, B.R.T., 2009. Widespread Upper Triassic to Lower Jurassic wildfire records from

685   Poland: Evidence from charcoal and pyrolytic polycyclic aromatic hydrocarbons. Palaios 24, 785–798.

686   Matsumoto, R., Iijima, A. 1981. Origin and diagenetic evolutionof Ca-Mg-Fe carbonates in some coalfields

687   of Japan. Sedimentology 28, 239–259.

688   McElwain, J.C., Beerling, D.J., Woodward, F.I. 1999. Fossil plants and global warming at the Triassic –

689   Jurassic boundary. Science 285, 1386–1390.

690   Metcalfe, I. 2011. Tectonic framework and Phanerozoic evolution of Sundaland. Gondwana Research 19, 3–

691   12.

692   Mogensen, T. E., Kortsgård, J. A. 2003. Triassic and Jurassic transtension along part of the Sorgenfrei–

693   Tornquist Zone in the Danish Kattegat. In: Ineson, J. R., Surlyk, F. (Eds.), The Jurassic of Denmark and

694   Greenland. Geological Survey of Denmark and Greenland Bulletin 1, 439–458.

695   Mortimer, R. J. G., Coleman, M. L., Rae, J. E. 1997. Effect of bacteria on the elemental composition of early

696   diagenetic siderite: implications for palaeoenvironmental interpretations. Sedimentology 44, 759–765.

697   Mozley, P.1989. Relation between depositional environment and the elemental composition of early

698   diagenetic siderite. Geology 17, 704–706.

699   Mozley, P. S., Carothers, W. W. 1992. Elemental and isotopic composition of siderite in the Kuparuk

700   Formation, Alaska: Effect of microbial activity and water/sediment interaction on early pore-water

701   chemistry. Journal of Sedimentary Petrology 62, 681–692.

702   Mozley, P. S., Wersin, P. 1992.Isotopic composition of siderite as an indicator of depositional environment.

703   Geology 20, 817–820.

704   Nielsen, L. H. 2003. Late Triassic-Jurassic development of the Danish Basin and the Fennoscandian Border

705   Zone, southern Scandinavia. In: Ineson, J. R., Surlyk, F. (Eds.), The Jurassic of Denmark and Greenland.

706   Geological Survey of Denmark and Greenland Bulletin, 459–526.

707   Petersen, H. I., Lindström, S. 2012. Synchronous wildfire activity rise and mire deforestation at the Triassic-

708   Jurassic boundary. PLoS One 7(10) e47236.doi:10.1371, 15pp.

709   Petersen, H. I., Lindström, S., Therkelsen, J., Pedersen, G. K. 2013. Deposition, floral composition and

710   sequence stratigraphy of uppermost Triassic /Rhaetian) coastal coals, southern Sweden. International Journal

711   of Coal Geology 116-117, 117–134.

712   Pott, C., McLoughlin, S. 2011. The Rhaetian flora of Rögla, northern Scania, Sweden. Palaeontology 54,

713   1025–1051

714   Retallack, G.J. 1997. Paleosols in the Upper Narrabeen group of New South Wales as evidence of Early

715   Triassic palaeoenvironments without exact modern analogues. Australian Journal of Earth Sciences 44, 185–

716   201.

717   Robinson, S. A., Scotchman, J. I., White, T. S., Atkinson, T. C. 2010. Constraints on palaeoenvironments in

718   the Lower Cretaceous Wealden of southern England, from the geochemistry of sphaerosiderites. Journal of

719   the Geological Society, London, 167, 303–311.

720   Rosenbaum, J. M., Sheppard, S. M. F. 1986. An isotopic study of siderites, dolomites and ankerites at high

721   temperatures. Geochimica et Cosmochimica Acta 50, 1147–1150.

722   Rosenau, N. A., Tabor, N. J., Elrick, S. D., Nelson, J. W. 2013. Polygenetic history of paleosols in Middle –

723   Upper Pennsylvanian cyclothems of the Illinois Basin, U.S.A.: Part I. Characterization of paleosol types and

724   interpretation of pedogenic processes. Journal of Sedimentary Research 83, 606–636.

725   Ruhl, M., Bonis, N. R., Reichart, G.-J., Damsté, J. S., Kürschner, W. M. 2011. Atmospheric carbon injection

726   linked to end-Triassic mass extinction. Science 233, 430–434.

727   Schoene, B., Guex, J., Batrtolini, A., Schaltegger, U., Blackburn, T. J. 2010. Correlating the end-Triassic

728   mass extinction and flood basalt volcanism at the 100 ka level. Geology 38, 387–390.

729   Sholkovitz, E. R., Copland, D. 1981. The coagulation, solubility and adsorption properties of Fe, Mn, Cu, Ni,

730   Cd, Co and humic acid in river water. Geochimica et Cosmochimica Acta 45, 181–189.

731   Sivhed, U. 1984: Litho- and biostratigraphy of the Upper Triassic-Middle Jurassic in Scania, southern

732   Sweden. Sveriges geologiska Undersökning, Ser. C, No. 806, 31 pp.

733   Steinthorsdottir, M., Woodward, F. I., Surlyk, F., McElwain, J. C. 2012. Deep-time evidence of a link

734   between elevated CO_2 concentrations and perturbations in the hydrological cycle via drop in plant

735   transpiration. Geology 40, 815–818. Suarez, M. B., González, L. A., Ludvigson, G. A. 2010. Estimating the

736   oxygen isotopic composition of equatorial precipitation during the Mid-Cretaceous. Journal of Sedimentary

737   Research 80, 480–491.

738   Topal, S., Özkul, M. 2014. Soft-sediment deformation structures interpreted as seismites in the Kolankaya

739   Formation, Denizli Basin (SW Turkey). The Scientific World Journal 2014,

740   dx.doi.org/10.1155/2014/352654, 13pp.

741   Troedsson, G. 1951. On the Höganäs series of Sweden (Rhaeto-Lias). Lunds Universitets Årsskrift, N. F. 47,

742   269p.

743   Ufnar, D. F., Gonzáles, L. A., Ludvigson, A., Brenner, R. L., Witzke, B. J. 2001. Stratigraphic implications

744   of meteoric sphaerosiderite δ^{18}O values in paleosols of the Cretaceous (Albian) Boulder Creek Formation,

745   NE British Columbia Foothills, Canada. Journal of Sedimentary Research 71, 1017–1028.

746   Ufnar D. F., Gonzáles, L.A., Ludvigson, G.A., Brenner, R.L., Witzke, B.J. 2002. The mid-Cretaceous water

747   bearer: isotope mass balance quantification of the Albian hydrologic cycle. Palaeogeography,

748   Palaeoclimatology, Palaeoecology 188, 51–71.

749   Ufnar, D.F., Ludvigson, G.A., Gonzáles, L.A.,Brenner, R.L., Witzke, B.J. 2004a. High latitude meteoric

750   δ^{18}O compositions: paleosol siderite in the mid-Cretaceous Nanushuk Formation, North Slope Alaska.

751   Geological Society of America Bulletin 116, 63–159.

752   Ufnar, D. F., González, L. A., Ludvigson, G. A., Brenner, R. L., Witzkes, B. J. 2004b. Diagentic

753   overprinting of the sphaerosiderite palaeoclimate proxy: are records of pedogenic groundwater δ^{18}O values

754   preserved? Sedimentology 51, 127–144.

755   van de Schootbrugge, B., Quan, T. M., Lindström, S., Püttmann, W., Heunisch, C., Pross, J., Fiebig, J.,

756   Petschick, R., Röhling, H.-G., Richoz, S., Rosenthal, Y., Falkowski, P. G. 2009. Floral changes across the

757   Triassic/Jurassic boundary linked to flood basalt volcanism. Nature Geoscience 2, 589–594.

758   Van Houten, F. B. 1961. Climatic significance of red beds. In: Nairn, A. E. M (Ed.) Descriptive

759   palaeoclimatology. Interscience Publishers Inc, New York, 89–139.

760   Wang, C.-Y., Manga, M. 2010. Hydrologic responses to earthquakes and a general metric. Geofluids 10,

761   206–216.

762   Weibel, R. 1999. Effects of burial on the clay assemblage in the Triassic Skagerrak Formation. Clay

763   Minerals 34, 619–635.

764   Weibel, R., Friis, H., Kazerouni, A. M., Svendsen, J. B., Stokkendahl, J., Poulsen, M. L. 2010. Development

765   of early diagenetic silica and quartz morphologies – Examples from the Siri Canyon, Danish North Sea.

766   Sedimentary Geology 228, 151–170.

767   Wilkinson, M., Haszeldine, R. S., Fallick, A. E., Osborne, M. J. 2000. Siderite zonation within the Brent

768   Group: microbial influence or aquifer flow? Clay Minerals 35, 107–117.

769

770   Figure captions

771

772   **Table 1.**

773   Sphaerosiderite occurrences, their geological background, morphology and geochemistry.

774

775   **Fig. 1.**

776   Stratigraphy of southern Sweden, which is compared with changes in sphaerosiderite occurrence (Troedsson

777   1951 and this study), dominating clay mineralogy (Ahlberg et al. 2003), occurrence of coal and remnants

778   after wildfire activity (Troedsson 1951; Petersen and Lindström 2012) and palynozones (Lund 1977 and this

779   study). Transgressive events are indicated (arrows), including MFS7, which is an important surface for

780   correlation in the region (Nielsen 2003).

781

782   **Fig. 2.**

783   Map showing location of the Norra Albert quarry and the wells Albert-1 and Fleninge No. 266. Note that the

784   position of the Norra Albert quarry and the Albert-1 well are identical.

785

786   **Fig. 3.**

787   Sedimentary logs showing typical siderite morphologies for the investigated samples.

788   A. Sedimentary log of the northern wall in the Norra Albert quarry.

789   B. Sedimentary log of the Albert-1 core.

790   C. Constructed sedimentary log of the Fleninge No. 266 well based on the description by Troedsson

791   (1951).

792   Dimensions given in the diagrams are those of sphaerosiderite, spheroidal and rhombohedral siderite, not the

793   dimensions of the concretions.

794

795

796 **Fig. 4. Fieldwork Norra Albert quarry.**

797   A. Overview of the northern wall in Norra Albert quarry. The 'Boserup beds' are the whitish grey

798   deposits with local siderite concretions; the dark grey deposits of the Bjuv Member are partly

799   covered by scree. The line marks the boundary between the 'Boserup beds' and the Bjuv Member.

800   Arrows indicate some of the largest concretions.

801   B. Petrified wood enclosed in a siderite concretion.

802   C. Undulating siderite concretion following the sedimentary structures.

803   D. Close up of A.

804   E. Thick siderite concretion with a middle plane following the sedimentary structures, similar to the

805   concretionary development in C, and surrounded by growth that cuts the sedimentary structures.

806   Thegrowth probably started along the most coarse-grained sands and continued both upwards and

807   downwards into the more fine-grained sandstones.

808   F. Close up of white box in E. The sedimentary structures seem to end at the concretionary interface,

809   but thin section investigations have shown that sedimentary structures actually continue through the

810   cemented area.

811

812 **Fig. 5.** An early displacive growth of siderite is documented by the high siderite content in concretions

813 compared with sandstones in the Norra Albert quarry. The mineral content is calculated from chemical

814 composition of bulk rock samples.

815

816 **Fig. 6. Poorly zoned sphaerosiderites (spherulites, spherulitic siderite)**

817   A. Poorly zoned sphaerosiderite (Si) with a low content of Ca and/or Mn commonly having central

818   dissolution voids (marked by black arrows). Norra Albert quarry, 516816. Back –scatter electron

819   (BSE) image.

820   B. Poorly zoned sphaerosiderite (Si) with incipient dissolution in the centre and rims of dissolution void

821   around the central spherical part. The most intensive dissolution accompanies the centre having a

822   small Ca content (compare EDS analyses 1 and 2). Norra Albert quarry, 516807. BSE image.

823   C. Poorly zoned sphaerosiderite (Si) with central dissolution void containing possible authigenic quartz

824   (Q) and un-compacted kaolinite (Ka) and surrounded by compacted kaolinite. Fleninge No. 266,

825   151.62 m. BSE image.

826   D. Poorly zoned sphaerosiderite (Si) (EDS analysis 3) with a centre possibly made up of iron-

827   oxide/hydroxide (Fe-ox) having a low content of Mn (EDS analysis 4). Norra Albert quarry, 516824.

828   BSE image.

829

830   **Fig. 7. Perfectly zoned sphaerosiderites**

831   A. Zoned sphaerosiderites replaced by iron-oxides/hydroxides (Fe). Note that the sphaerosiderite at

832   some point has lost contact to their growth substratum, however this has healed later. Norra Albert

833   quarry, 516818. Reflected light image.

834   B. Broken perfectly zoned sphaerosiderite with healing rhombohedral siderite that appears the same as

835   the overgrowth on the sphaerosiderite. Later exposure to oxidising water has resulted in replacement

836   by iron-oxides/hydroxides (Fe). Norra Albert quarry, 516818. BSE image.

837   C. Microcrystalline anhedral siderite (Si) tightly fills the pore space between the sphaerosiderite and

838   detrital grains. The detrital grains (Q) are dispersed and do not exhibit intergranular contacts, which

839   indicate displacive and/or replacive growth of siderite. Alteration and replacement by iron-

840   oxides/hydroxides (Fe) is probably related to oxidation of siderite along fracture wall probably due

841   to percolation of oxygenated fluids. Norra Albert quarry, 516824D. BSE image.

842   D. Zoned sphaerosiderites replaced by iron-oxides/hydroxides (Fe). Altering zones seem to be almost

843   similar for a specific area/concretion. The apparent variation in zonation pattern may be caused by

844   different intersection planes. Norra Albert quarry, 516818. BSE image.

845   E. Fine-crystalline morphology of the inner part of the sphaerosiderite, which is ripped out, and coarser

846   crystals as an outer rim. Norra Albert quarry, 516818. Secondary electron (SE) image.

847   F. Rhombohedral habit of siderite crystals forming an overgrowth on the sphaerosiderite. Norra Albert

848   quarry, 516818. SE image.

849

850   **Fig. 8. Varieties of zoned sphaerosiderites**

851   A.   Sphaerosiderite with relatively high content of Mn in the inner core (EDS analysis 1), followed by a

852   rhodochrosite rim (EDS analysis 2) with dissolution voids (white arrows) and an outermost rim of

853   low-Mn siderite . Norra Albert quarry, 516819. BSE image.

854   B.   Cluster of rhodochrosite rimed sphaerosiderite enclosed in sparry siderite cement. Norra Albert

855   quarry, 516819. SE image.

856   C.   Concentric and sector zoned sphaerosiderite having a low content of Ca (EDS analysis 3), whereas

857   the alteration rims show siderite with low contents of Si and possible Zn (EDS analysis 4). Norra

858   Albert quarry, 516820. BSE image.

859   D.   Round siderite core covered by rhombohedral siderite, which is partly dissolved and altered to iron-

860   oxides/hydroxides. Norra Albert quarry, 516825. SE image.

861

862   **Fig. 9. Spheroidal siderite (pseudomorphs after stomata)**

863   A.   Spheroidal siderite with radiating growth around a spheroidal core and in zones. Norra Albert

864   quarry, 516824C. Transmitted light image, crossed nicols.

865   B.   Spheroidal siderite with marked spheroidal zones. Norra Albert quarry, 516824C. Reflected light

866   image.

867   C.   Spheroidal siderite with radiating growth in spheroidal zones. Acid treated sample, Norra Albert

868   quarry, 516824C. SE image.

869

870   **Fig. 10 Chemical composition**

871   Microprobe analyses show that siderite generally has a low content of Mg and Ca, though commonly

872   relatively high content of Mn. The highest Mn contents typically occur in spheroidal siderite, perfectly zoned

873   sphaerosiderite and their overgrowths, whereas the highest Ca contents occur in poorly zoned

874   sphaerosiderite.

875

876

877 **Fig. 11. Isotopic composition**

878   A. IRMS (isotope ratio mass spectrometry) shows a narrow $\delta^{18}O$ composition and a large span in $\delta^{13}C$

879   values for bulk rock samples. Also perfectly zoned sphaerosiderite with zones of rhodochrocite

880   groups together with other siderite samples.

881   B. SIMS (secondary ion mass spectrometry) of specific siderite morphologies in thin sections shows

882   that perfectly zoned sphaerosiderite, spheroidal siderite and their siderite overgrowths have similar

883   and lower $\delta^{13}C$ values than the siderite concretionary cement.

884 SIMS and IRMS analyses show similar $\delta^{18}O$ values for all siderite micromorphologies and the

885 concretionary cement, which reflect end-Triassic groundwater composition. This fits with the likely

886 meteoric water composition (indicated by the vertical blue lines) according to the Triassic – Jurassic

887 middle latitude position at 45°N of Sweden (Anderson and Arthur 1983; Metcalfe 2011; Blakey 2016).

888

889 **Fig. 12. Overview of siderite precipitation**

890 Diagram showing an overview of the precipitation and growth of the different siderite morphologies in

891 relation to other diagenetic features.

892

893

894

895

Figure captions
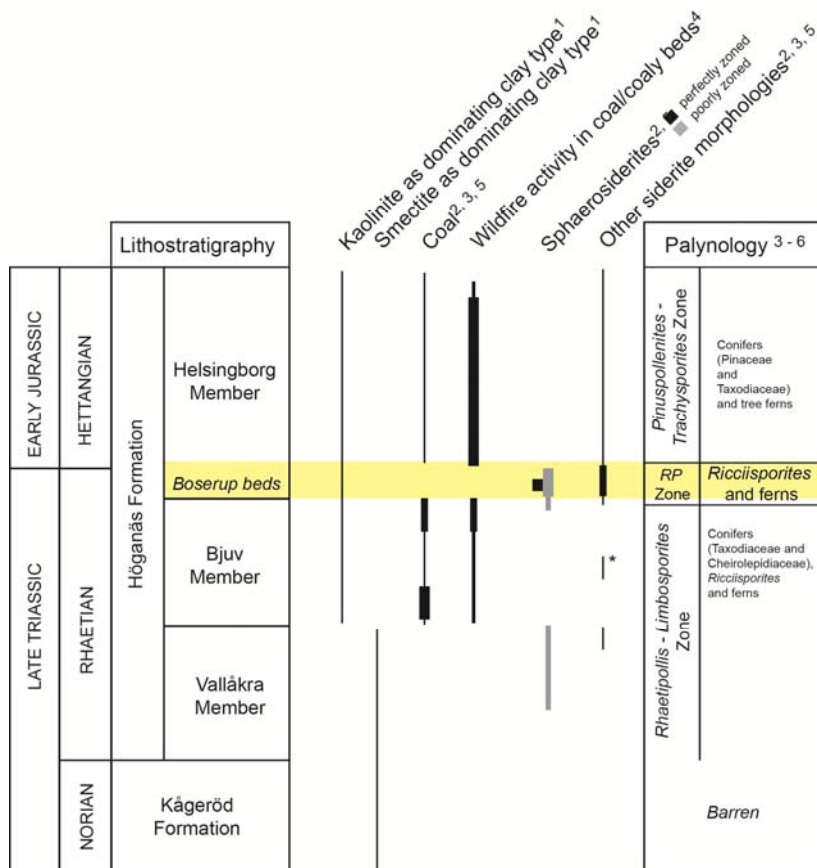
[1] Ahlberg et al. 2003
[2] Troedsson 1951
[3] Lindström and Erlström 2006
[4] Petersen and Lindström 2012
[5] Lund 1977
[6] This paper

Fig. 1.

Stratigraphy of southern Sweden based on changes in sphaerosiderite occurrence (Troedsson 1951 and this study), dominating clay mineralogy (Ahlberg et al. 2003), occurrence of coal and remnants after wildfire activity (Troedsson 1951; Petersen and Lindström 2012) and palynozoes (Lund 1977 and this study). Transgressive events are indicated (arrows), including MFS7, which is an important surface for correlation in the region (Nielsen 2003).
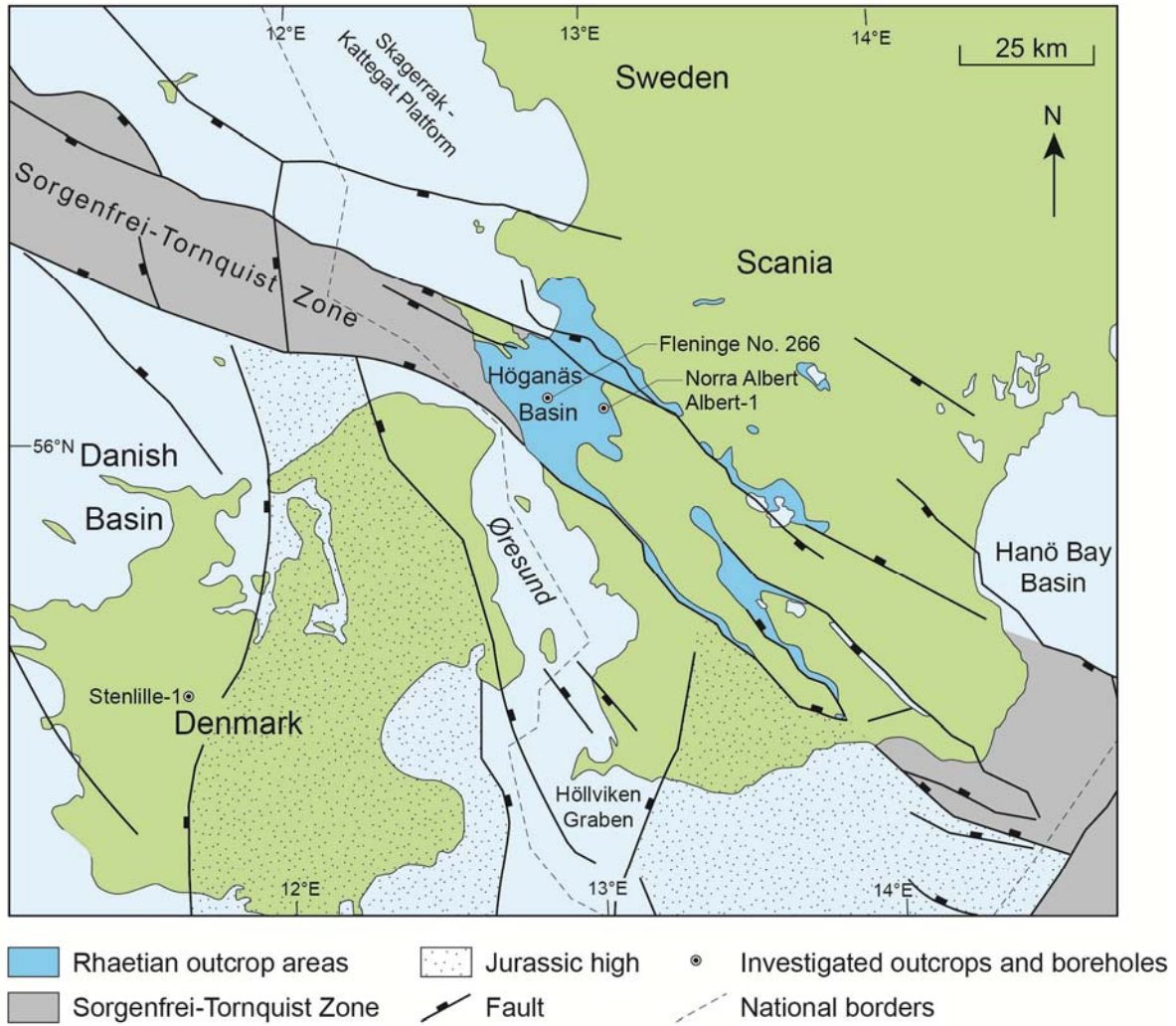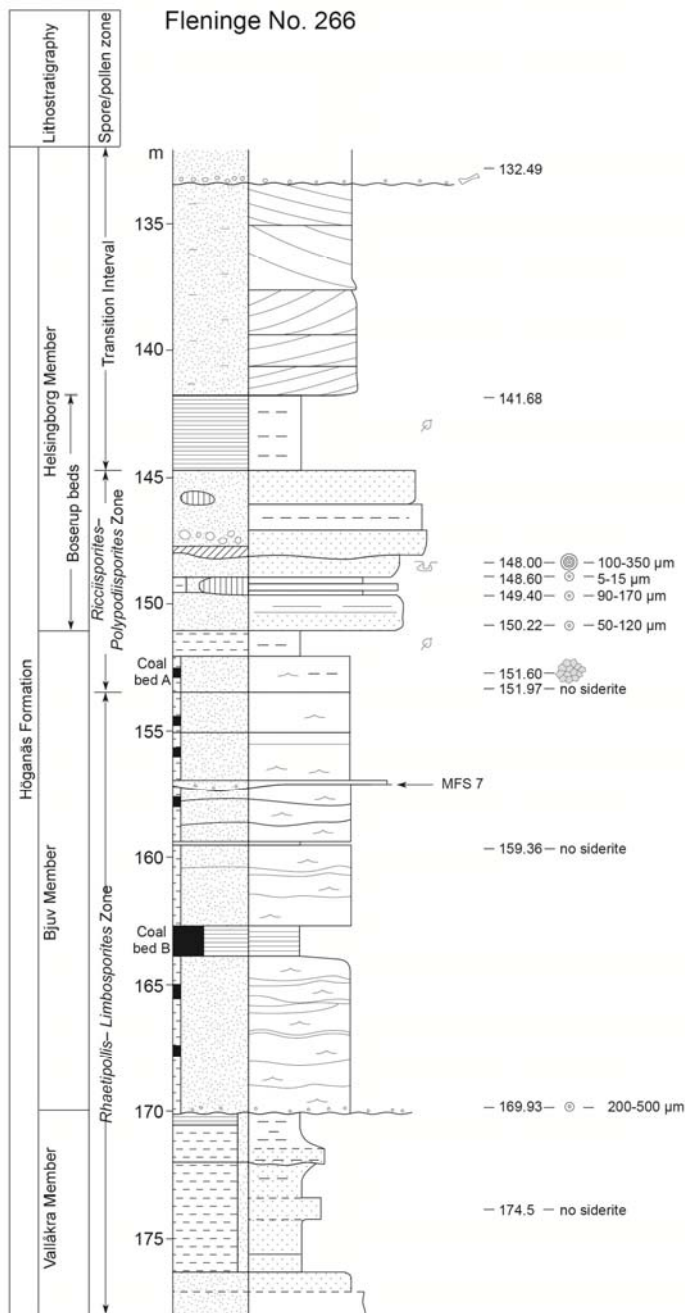
Fig. 2.

Map showing location of the Norra Albert quarry and the wells Albert-1 and Fleninge No. 266. Note that the position of the Norra Albert quarry and the Albert-1 well are identical.
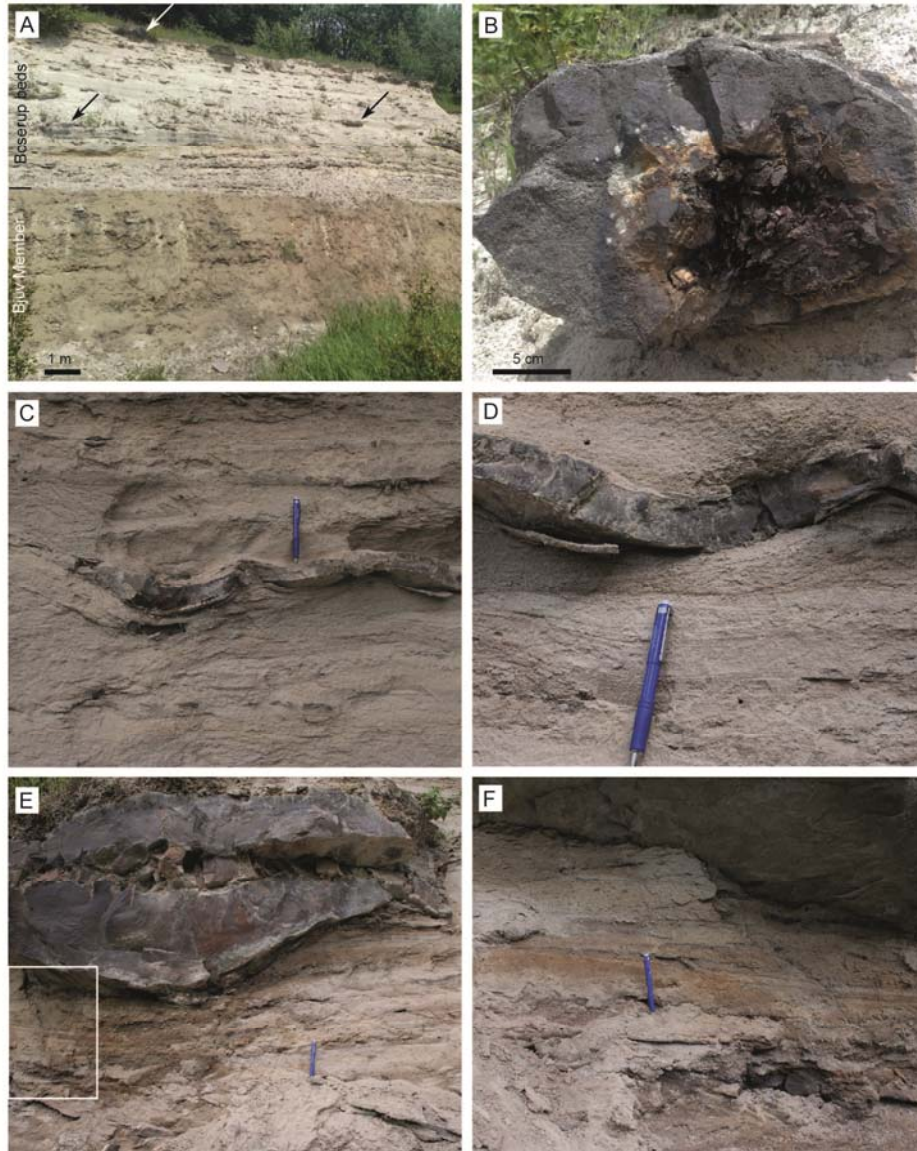
Norra Albert

Lithology	
	Sand
	Silt
	Clay
	Coal
	Coal clasts
	Intraformational clasts
	Concretion

Sedimentary structures

	Lamination
	Weak lamination
	Undulatory lamination
	Flaser bedding
	Cross-lamination
	Wave-ripple cross-lamination
	Planar cross-bedding
	Trough cross-bedding
	Hummocky cross-stratification
	Structureless
	Soft sediment deformation structures

Trace fossils and biota

	Weak to intense bioturbation
	Plant remains
	Bone fragments
	Rootlet
	Teichichnus isp.
	Chondrites isp.

Albert-1

Lithostratigraphy

Bjuv Member

Höganäs Formation

Valläkra Member

Kågeröd Fm

Floor of quarry

AL1-03.92 — no siderite
AL1-05.17 — no siderite
AL1-06.95 — no siderite
AL1-07.72 — no siderite
AL1-09.28 —
AL1-10.89 —
AL1-11.47 — no siderite
AL1-12.55 — no siderite
AL1-14.81 — no siderite
AL1-15.05 — ⊙ — ~5 µm

Fig. 3.

Sedimentary logs showing typical siderite morphologies for the investigated samples.

A. Sedimentary log of the northern wall in the Norra Albert quarry.

B. Sedimentary log of the Albert-1 core.

C. Constructed sedimentary log of the Fleninge No. 266 well based on the description by Troedsson (1951).

Dimensions given in the diagrams are those of sphaerosiderite, spheroidal and rhombohedral siderite, not the dimensions of the concretions.

Fig. 4. Fieldwork Norra Albert quarry.

A. Overview of the northern wall in Norra Albert quarry. The 'Boserup beds' are the whitish grey deposits with local siderite concretions; the dark grey deposits of the Bjuv Member are partly covered by scree. The line marks the boundary between the 'Boserup beds' and the Bjuv Member.

B. Petrified wood enclosed in a siderite concretion.

C. Undulating siderite concretion following the sedimentary structures.

D. Close up of A.

E. Thick siderite concretion, which probably started along the most coarse-grained sands, similar to the morphology in C, and continued both upwards and downwards.

F. Close up of white box in E. The sedimentary structures seem to end at the concretionary interface, but thin section investigations have shown that sedimentary structures actually continue through the cemented area.
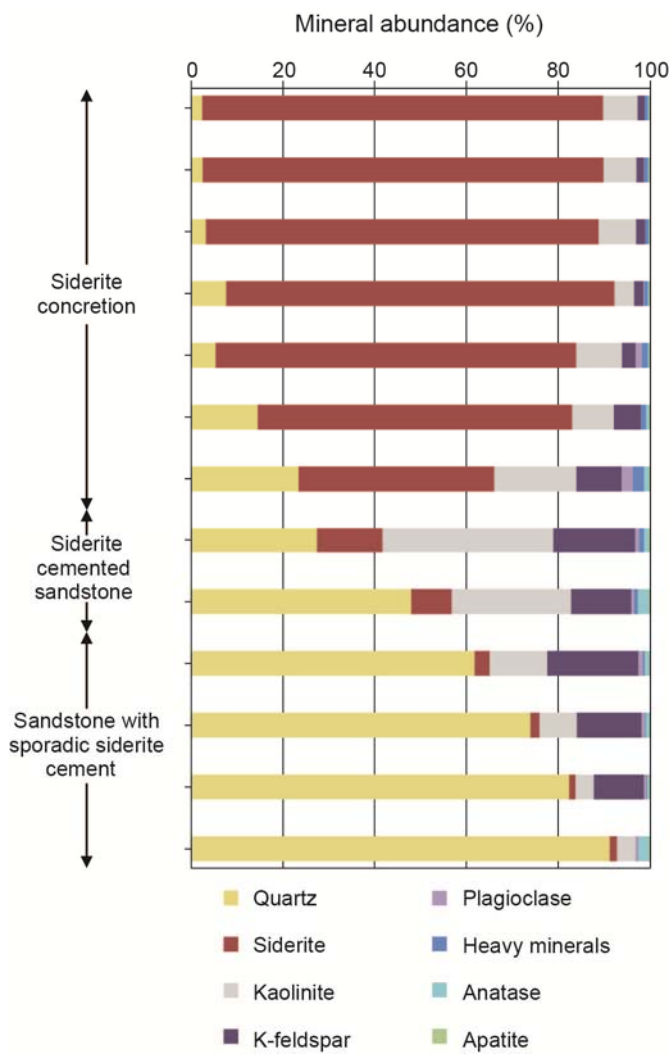
Fig. 5. An early displacive growth of siderite is documented by the high siderite content in concretions compared with sandstones in the Norra Albert quarry. The mineral content is calculated from chemical composition of bulk rock samples.
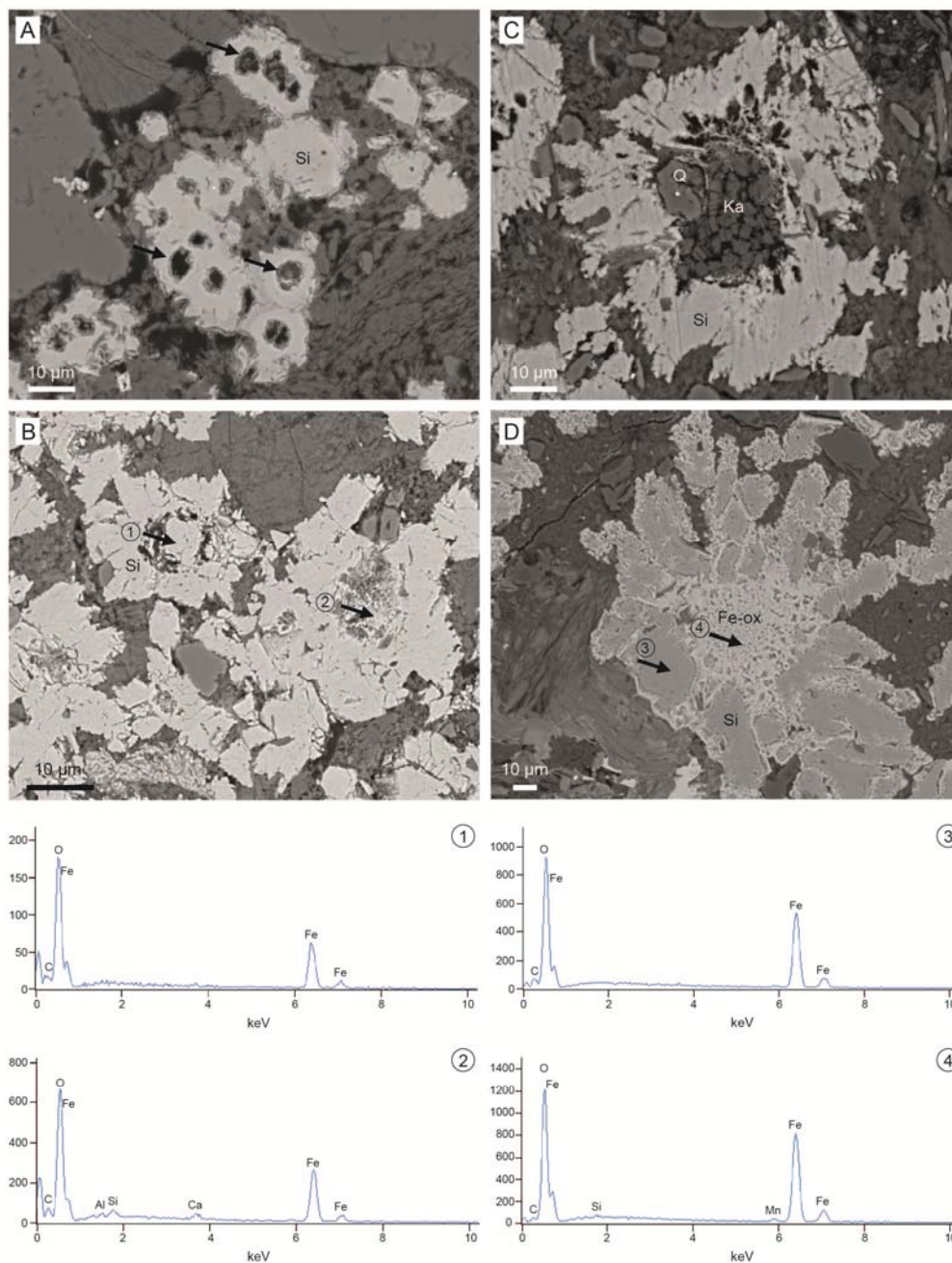
Fig. 6. Poorly zooned sphaerosiderites (spherulites, spherulitic siderite)

A. Poorly zoned sphaerosiderite. Norra Albert quarry, 516816. Back -scatteredelectron (BSE) image.

B. Poorly zoned sphaerosiderite with incipient dissolution in the centre and rims of dissolution void around the central spherical part. Norra Albert quarry, 516807. BSE image.

C. Poorly zoned sphaerosiderite with central dissolution void containing authigenic quartz (Q) and un-compacted kaolinite (Ka) and surrounded by compacted kaolinite. Fleninge No. 266, 151.62 m. BSE image.

D. Poorly zoned sphaerosiderite with a centre possibly made up of iron-oxide/hydroxide. Norra Albert quarry, 516824. BSE image.
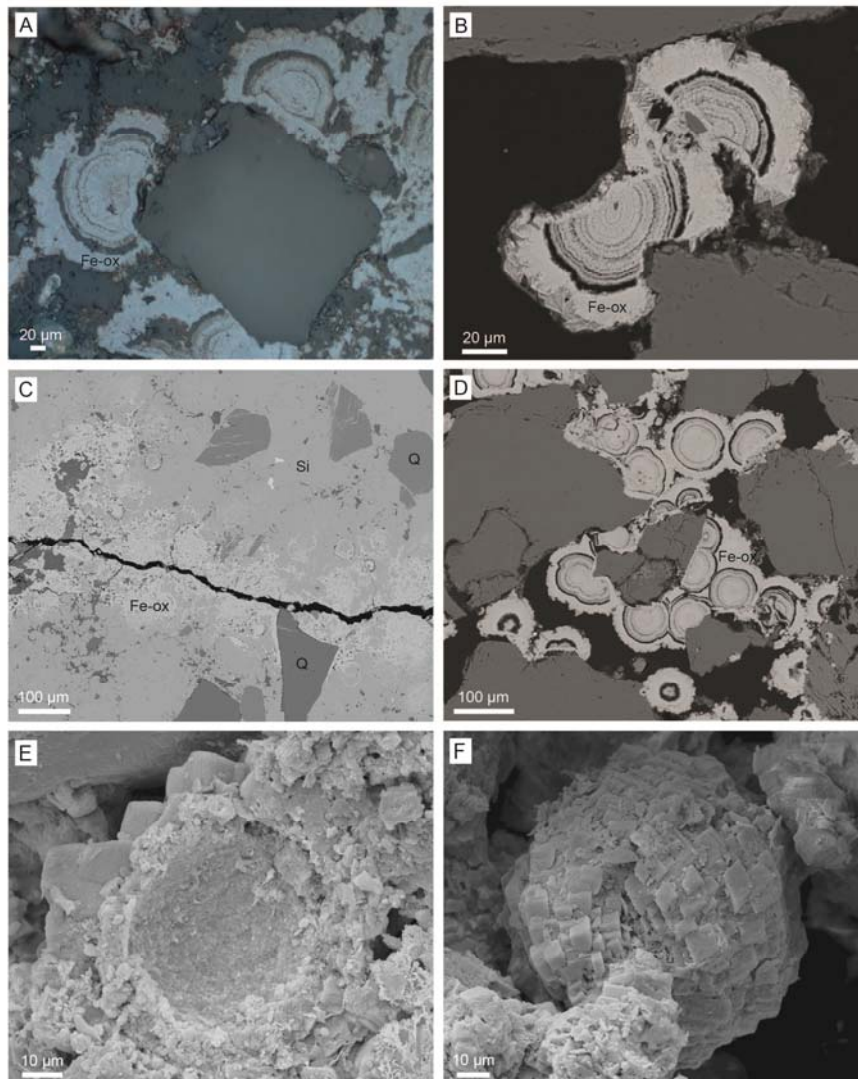
Fig. 7. Perfectly zoned sphaerosiderites

A. Zoned sphaerosiderites. Note that the sphaerosiderite at some point has lost contact to their growth substratum, however this has healed later. Norra Albert quarry, 516818. Reflected light image

B. Apparently poikilotopic siderite cement, which reveals the presence of sphaerosiderite along a fracture where alteration has penetrated. Norra Albert quarry, 516824D. BSE image.

C. Fine-crystalline morphology of the inner part of the sphaerosiderite, which is ripped out, and coarser crystals as an outer rim. Norra Albert quarry, 516818. Secondary electron (SE) image.

D. Broken perfectly zoned sphaerosiderite, which later has healed. Norra Albert quarry, 516818. BSE image.

E. Zoned sphaerosiderites. Altering zones seem to be similar for a specific area, here two different types of zonation is shown. Norra Albert quarry, 516818. BSE image.

F. Siderite crystals covering the sphaerosiderite. Norra Albert quarry, 516818. SE image.
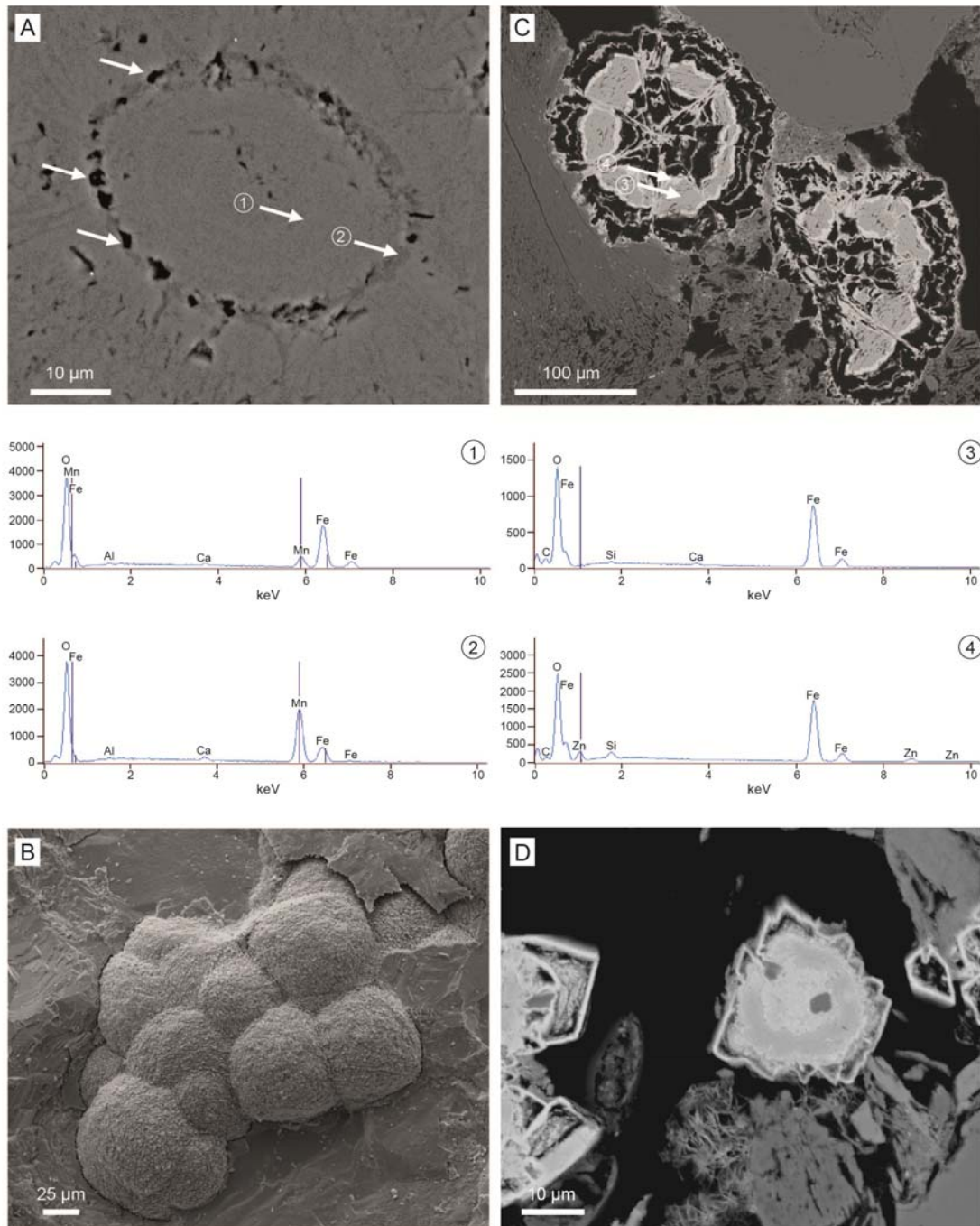
Fig. 8. Varieties of zoned sphaerosiderites

A. Rhodochrosite rim with dissolution voids marking one of the zones in sphaerosiderite. Norra Albert quarry, 516819. BSE image.

B. Cluster of rhodochrosite rimed sphaerosiderite enclosed in sparry siderite cement. Norra Albert quarry, 516819. SE image.

C. Concentric and sector zoned sphaerosiderite. Norra Albert quarry, 516820. BSE image.

D. Round siderite core covered by rhombohedral siderite. Norra Albert quarry, 516825. SE image.
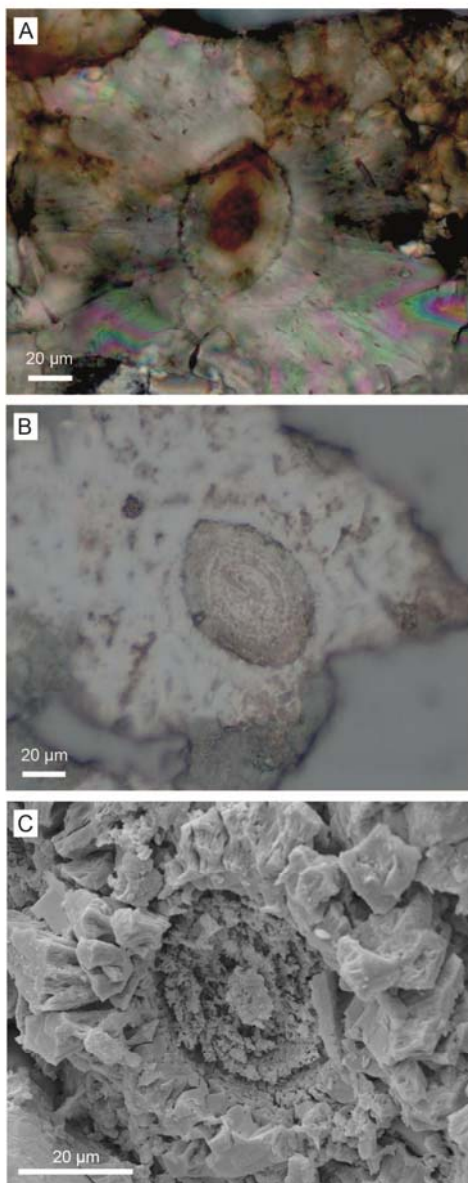
**Fig. 9. Spheroidal siderite (pseudomorphs after stomata)**

A. Spheroidal siderite with radiating growth around a spheroidal core and in zones. Norra Albert quarry, 516824C. Transmitted light image, crossed nicols.

B. Spheroidal siderite with marked spheroidal zones. Norra Albert quarry, 516824C. Reflected light image.

C. Spheroidal siderite with radiating growth in spheroidal zones. Acid treated sample, Norra Albert quarry, 516824C. SE image.
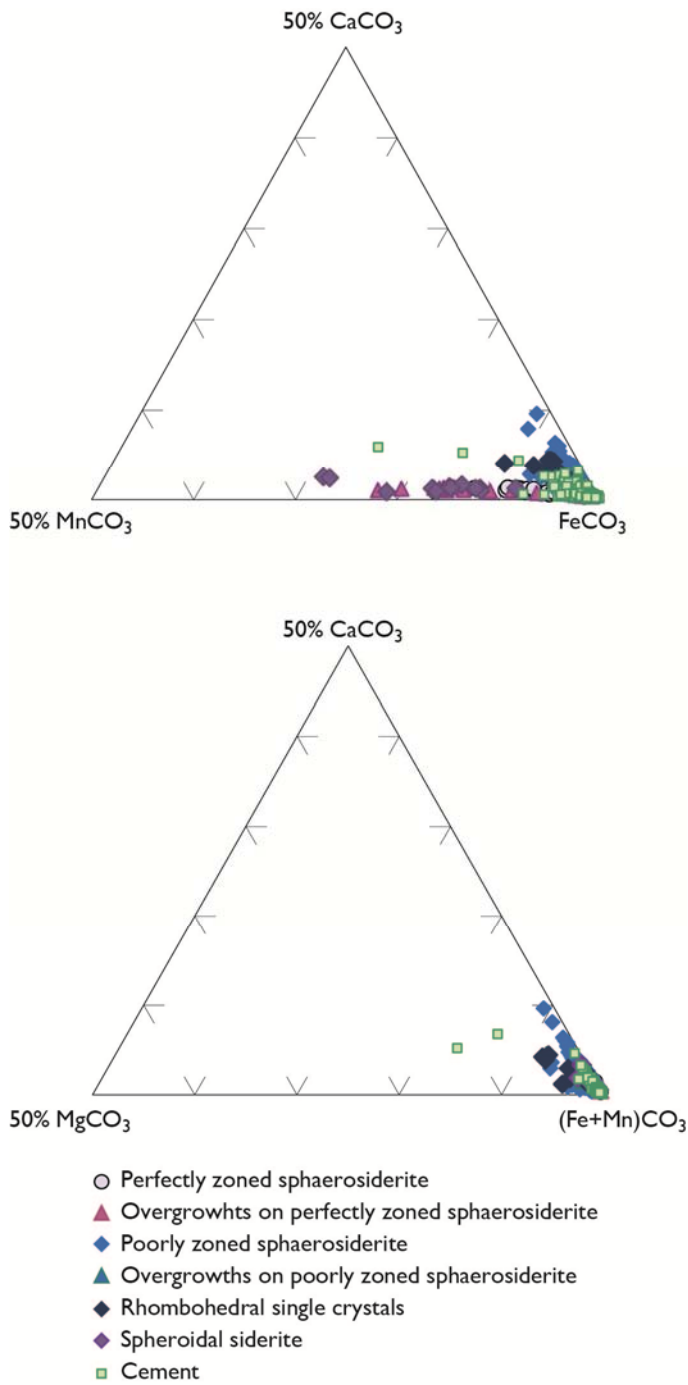
Fig. 10 Chemical composition

Microprobe analyses show that siderite generally has a low content of Mg and Ca, though occasionally relatively high content of Mn.
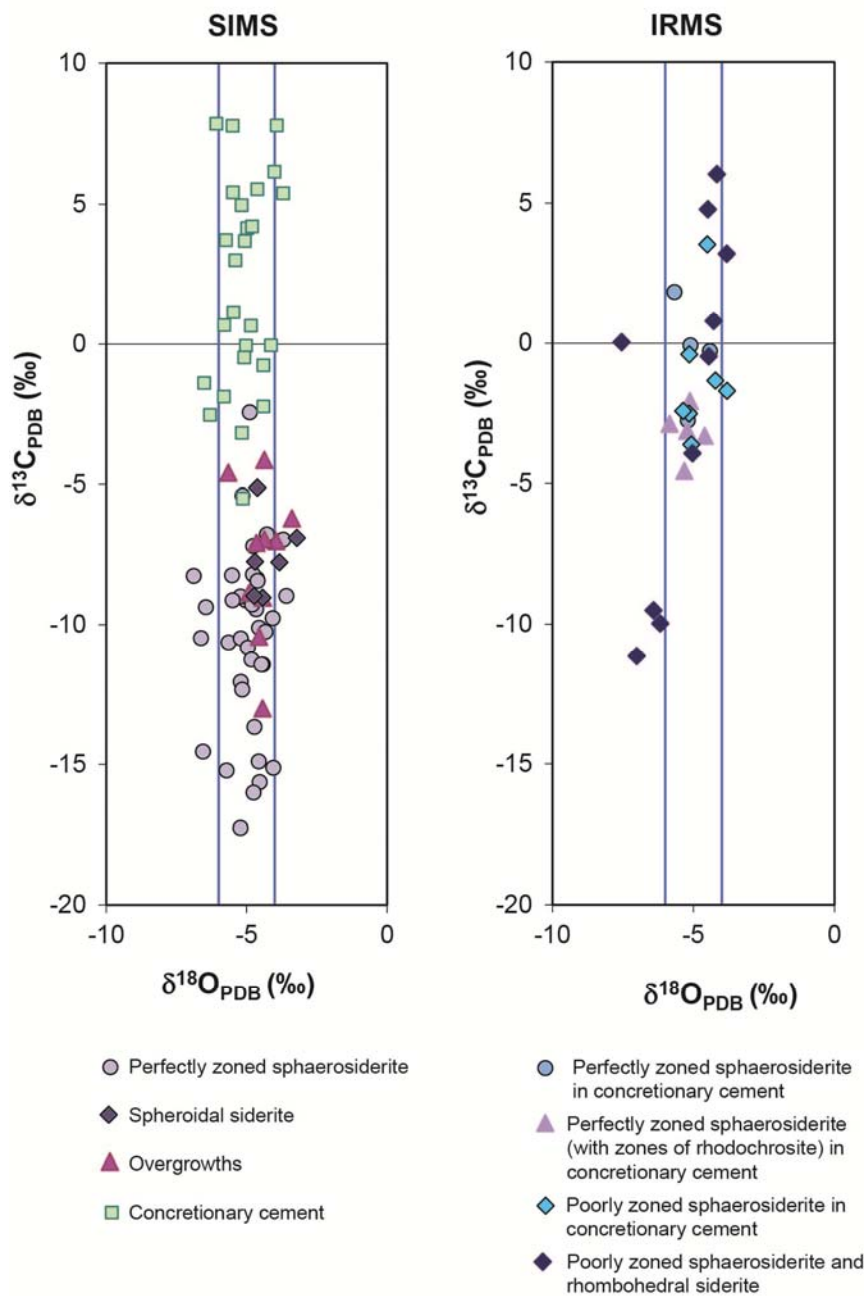
Fig. 11. Isotopic composition

The siderite isotopic composition measured by conventional mass spectrometry on bulk rock samples (bulk rock) and in specific siderite morphologies (*in situ*) by ion probe. Perfectly zoned sphaerosiderite and spheroidal siderite have similar and slightly lower $\delta^{13}C$ values than the siderite matrix. Bulk rock analyses of several samples show isotope values resembling those of *in situ* measurements of perfectly zoned sphaerosiderite, except weathered samples that have been exposed to more intensive alteration and replacement with iron-oxides/hydroxides.
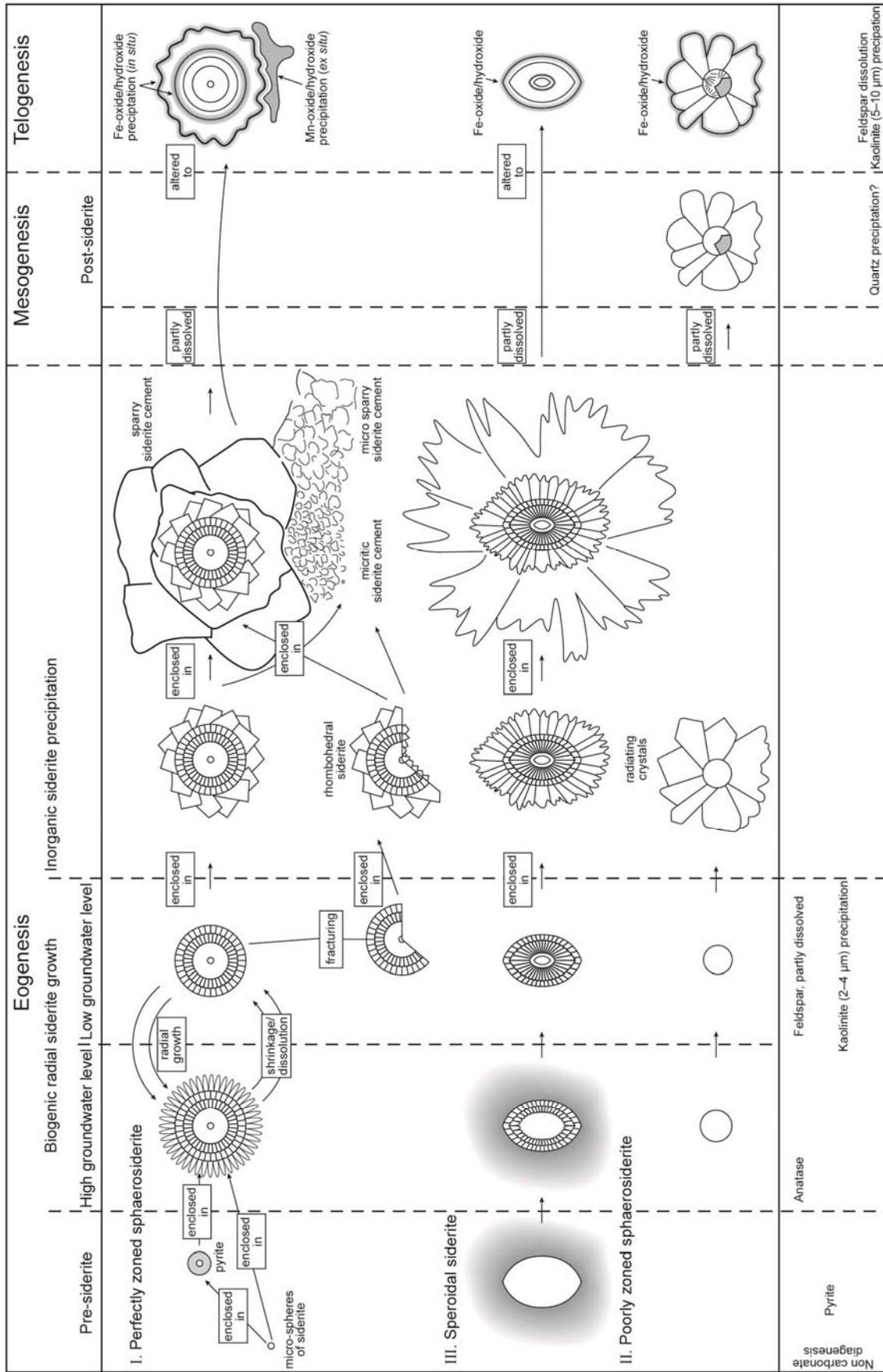
Fig. 12. Overview of siderite precipitation

Diagram showing an overview of the precipitation and growth of the different siderite morphologies in relation to other diagenetic features.